Chapter 4

Study of an arbitrary-oriented crack in bonded functionally graded strips

4.1 Mathematical study of an arbitrary-oriented crack crossing the interface of bonded functionally graded strips under thermo-mechanical loading

4.1.1 Introduction

Functionally graded materials (FGMs) are becoming more and more important due to the growing demand for composites and bonded materials in the modern technological era. This is because FGMs can reduce thermal and residual stresses and exhibit strong wear resistance, reliability at high temperatures, and other properties. FGMs are two-phase particle composites where the volume fraction of the constituents changes along the direction of thickness. FGMs with continuous mechanical

properties about the interface have been devised and manufactured in engineering over the years to increase the work reliability of composite interfaces and make material properties well-matched at the interface. The ability of composite structures to resist fracture can be improved with the use of these kinds of composite interfaces. More studies must be done on the fracture behavior of these non-homogeneous materials to technically support material scientists, manufacturing and design engineers, and others working on FGM development. The detailed examination of the driving forces of the crack is crucial for the fracture analysis of FGMs. This shows how effective the composition profile is at achieving the necessary thermo-mechanical properties.

The majority of study [5, 20, 47, 52, 90] has been done for the cracks those are vertical, parallel, and embedded in the interface or medium. In [102], the interaction between partially insulated cracks was studied for various specific cases of thermal, mechanical, and thermo-mechanical loadings using the mode I stress magnification factor. This analysis involved three collinear cracks in a functionally graded medium. The article [30] evaluated the effects of thermal loading on an interfacial crack in FGM strips by computing thermal stress intensity factors (TSIFs). Additionally, the nature of this partially insulated crack is explored concerning thermal resistance and material non-homogeneity factors. Inspection of the transient behavior of three anti-plane collinear Griffith cracks in a FGM strip under shear impact loading was the goal of [103]. The FGM strip has adhered between two different elastic strips of identical thickness. Additionally, the possibility of crack arrest for various fixed values of impact loads imposed at various surfaces, the locations of cracks' axes, and the thickness of the strips of the composite material are illustrated. In [48], the thermal fracture behavior of a vertical crack for a FGM-coating structure was examined analytically. Analysis was done on how geometric

parameters and non-homogeneity constants affected the TSIFs. The crack problem for a FGM strip under thermal stresses is done in [37].

The studies mentioned above focused on the issue of cracks that are either parallel or vertical to an interface or surface. These crack positions are very specific, though. The crack can generally be in any direction [34]. Because of this, it's crucial to look into arbitrarily oriented crack problems in FGMs. But the arbitrary-oriented crack problem in FGM strips, however, has not been extensively studied. For the fundamental solution of a single as well as many angled cracks in an infinite functionally graded plate, a general technique was developed in [99, 100] to calculate the impact of the driving force parameters, namely SIFs and SERRs. In [16], the heat conduction issue for an angled crack in an infinite functionally graded material was examined. The nature of the crack is assumed to be partially insulated in the investigation under a uniform heat flow. To analyze the impact of crack orientation and its interaction with grading inhomogeneity, the temperature gradient, and heat flow intensity factors were examined using the collocation technique. The identical problem with a perfectly insulated crack has been covered in [110]. The crack is located in an infinite functionally graded medium in each of these studies. However, it is possible to find an arbitrary-oriented crack in more than one medium and FGM strips. The impact of graded coatings on a thermally-induced oblique fracture located in a homogenous substrate while subject to mechanical loading was taken into account in [19]. The fracture problem of a crack in functionally graded strips in the presence of mechanical loading was inspected in [47], in which the possibility of crack passing through the interface of the said composite structure is also discussed along with the study of SIF for different material non-homogeneity constants, normalized crack length, and orientation angle. In [49], a similar issue was investigated for an arbitrary-oriented crack. The idea of dislocation density functions has been applied

to determine the unknowns in these studies.

The problem of a partially insulated crack in a composite structure made up of two functionally graded strips is taken into consideration in the current work. The crack is arbitrary-oriented and subjected to thermo-mechanical loading (see Figure 4.1.1). Fracture-related failure in FGMs can occur in a number of different ways [34]. One of those is failure brought on by a crack that can cross the interface of the chosen composite structure. It is noted in [63] that a crack in PSZ/superalloy FGMs can propagate across the interface between various layers. Similar phenomena were noted in the experiment of thermal shock performance of W/Cu FGM [69]. These experiments demonstrate how crucial it is to take into account the problem in which crack can go through the interface [47, 49]. But relatively few studies take into account this kind of crack problem. As a result, it is anticipated in this study that the crack may cross the interface of the aforementioned model. The thermal and mechanical parametric functions are approximated by exponential functions under the assumption that there is no interaction between the two. The heat conduction and plane elasticity equations, when subjected to the proper boundary-continuity conditions, are transformed into Fredholm type singular integral equations of the first kind employing the superposition technique and integral transformation. The temperature jump and displacements across the crack surfaces are the unknown variables of the integral equations, and they can be approximated by a series of Jacobi polynomials. The residue theorem and Schmidt method are used to obtain the solution of the singular integral equation. This approach differs from the works listed above in which the dislocation density functions are the unknown variables. It is not necessary to consider singular integral equations' unknown variables as dislocation density functions when applying the Schmidt method. The benefit of this approach is that by taking into account the initial few terms of the infinite series

of Jacobi polynomials, it works satisfactorily. The expressions of SIFs obtained from the Schmidt method help to determine mode I and mode II strain energy release rate (SERR) at the crack tips. The significant aspect of the chapter is the investigation of thermo-mechanical loading on driving force parameters that help to study the nature of arbitrary-oriented crack when it crosses the interface of the considered composite structure. A comparison between the current findings and those from previous studies [47] for a specific example is also provided to support the validity of the current study. An effort has been made to quantify the impact of the crack insulation parameter, crack orientation angle, strip thickness, and non-homogeneity parameters on mode I and mode II SIFs and SERRs in the vicinity of crack tips.

4.1.2 Mathematical formulation of the problem

4.1.2.1 Schematic description

Figure 4.1.1 depicts the schematic representation of the problem with the bonded functionally graded strips. The upper and the lower FGM strips are indicated by notations (I) and (II), respectively and their thickness is taken to be h_1 and h_2, respectively. The regions $\{0 \leq x \leq h_1, -\infty < y < \infty\}$ and $\{h_1 \leq x \leq h_1+h_2, -\infty < y < \infty\}$ in global coordinate system xoy are thought to be occupied by the FGM strips (I) and (II). The origin o of the global coordinate system xoy is placed at the top surface of the upper FGM strip whereas the origin o_0 of the local coordinate system $x_0o_0y_0$ has coordinates (x_c, y_c) in the global coordinate system xoy. In the local coordinate system $x_0o_0y_0$, an angled partially insulated crack of length (b_0-a_0) is oriented along the x_0-axis. The angle between x_0 and x-axis is symbolized by θ.

In this study, two different loads are taken into account, a steady-state heat flux Q_0 applied in the x-direction and external mechanical loads applied to the crack

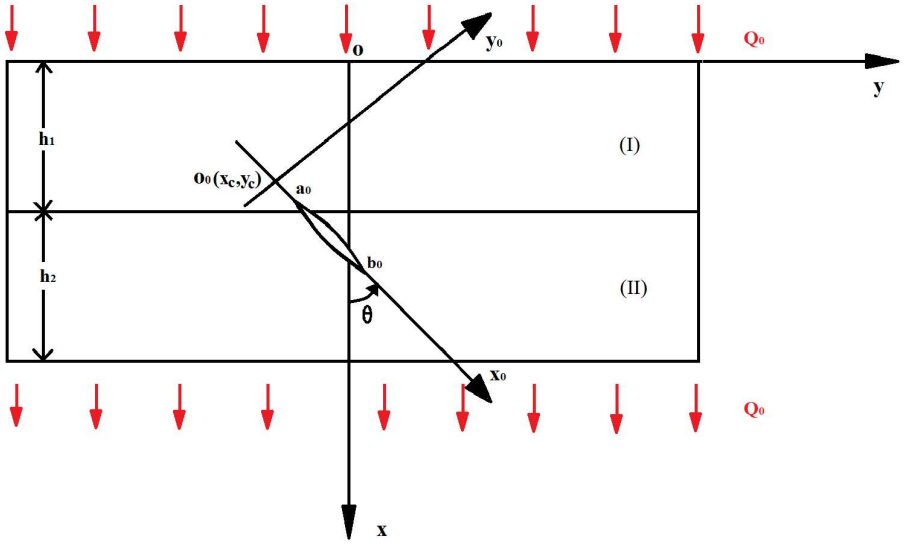

Figure 4.1.1: Schematic diagram of the problem.

faces. A constant value of the Poisson's ratio ν is used throughout the investigation due to the small variation range [28, 102]. The thermal and mechanical parametric functions namely, heat conductivity coefficients k_n, shear moduli μ_n and thermal expansion coefficients α_n are approximated by an exponential function [16, 30, 48, 102] in the global coordinate system as

$$k_n(x) = k_{0n}e^{\delta_n x}, \qquad \mu_n(x) = \mu_{0n}e^{\beta_n x}, \qquad \alpha_n(x) = \alpha_{0n}e^{\gamma_n x}, \tag{4.1.1}$$

whereas the following relation is used to determine those in the local coordinate system.

$$\begin{bmatrix} x \\ y \end{bmatrix} = \begin{bmatrix} x_c \\ y_c \end{bmatrix} + \begin{bmatrix} \cos(\theta) & -\sin(\theta) \\ \sin(\theta) & \cos(\theta) \end{bmatrix} \begin{bmatrix} x_0 \\ y_0 \end{bmatrix}, \tag{4.1.2}$$

$$k_n(x_0, y_0) = k_{0n}e^{\delta_n x_c + \delta_{n1}x_0 + \delta_{n2}y_0}, \tag{4.1.3}$$

$$\mu_n(x_0, y_0) = \mu_{0n}e^{\beta_n x_c + \beta_{n1}x_0 + \beta_{n2}y_0}, \tag{4.1.4}$$

$$\alpha_n(x_0, y_0) = \alpha_{0n}e^{\alpha_n x_c + \alpha_{n1}x_0 + \alpha_{n2}y_0}, \tag{4.1.5}$$

$$\text{where} \quad \delta_{n1} = \delta_n \cos(\theta), \qquad \delta_{n2} = -\delta_n \sin(\theta), \tag{4.1.6}$$

$$\beta_{n1} = \beta_n \cos(\theta), \qquad \beta_{n2} = -\beta_n \sin(\theta), \tag{4.1.7}$$

$$\gamma_{n1} = \gamma_n \cos(\theta), \qquad \gamma_{n2} = -\gamma_n \sin(\theta), \tag{4.1.8}$$

δ_n, β_n and γ_n are the non-homogeneity parameters. Throughout the study, $n = 1, 2$ correspond to strip (I) and strip (II), respectively and thermo-mechanical parametric functions are continuous at the interface viz. $k_1(h_1) = k_2(h_1)$, $\mu_1(h_1) = \mu_2(h_1)$ and $\alpha_1(h_1) = \alpha_2(h_1)$.

4.1.2.2 Governing equations and boundary conditions

The temperature and stress fields can be represented as the sum of two states using the superposition approach. The first state corresponds to an uncracked composite structure whereas the second state represents a cracked composite structure. In the first state, the components of temperature, heat flux, displacement, and stress are denoted by $T_n^{(1)}(x, y)$; $q_{nx}^{(1)}(x, y), q_{ny}^{(1)}(x, y)$; $u_n^{(1)}(x, y), v_n^{(1)}(x, y)$; $\sigma_{nxx}^{(1)}(x, y)$, $\sigma_{nxy}^{(1)}(x, y)$, $\sigma_{nyy}^{(1)}(x, y)$, respectively and in the second state those are denoted by $T_n^{(2)}(x_0, y_0)$; $q_{nx_0}^{(2)}(x_0, y_0)$, $q_{ny_0}^{(2)}(x_0, y_0)$; $u_n^{(2)}(x_0, y_0)$, $v_n^{(2)}(x_0, y_0)$; $\sigma_{nx_0x_0}^{(2)}(x_0, y_0)$, $\sigma_{nx_0y_0}^{(2)}$ (x_0, y_0), $\sigma_{ny_0y_0}^{(2)}(x_0, y_0)$, respectively, where $n = 1, 2$. Therefore, the total temperature $T_n^{tot}(x, y)$, heat flux $q_{nx}^{tot}(x, y), q_{ny}^{tot}(x, y)$, displacement $u_n^{tot}(x, y), v_n^{tot}(x, y)$ and stress components $\sigma_{nxx}^{tot}(x, y)$, $\sigma_{nxy}^{tot}(x, y)$, $\sigma_{nyy}^{tot}(x, y)$ in the xoy coordinate system can be expressed as

$$T_n^{tot}(x, y) = T_n^{(1)}(x, y) + T_n^{(2)}(x_0, y_0), \tag{4.1.9}$$

$$\begin{bmatrix} q_{nx}^{tot}(x, y) \\ q_{ny}^{tot}(x, y) \end{bmatrix} = \begin{bmatrix} q_{nx}^{(1)}(x, y) \\ q_{ny}^{(1)}(x, y) \end{bmatrix} + \begin{bmatrix} \cos(\theta) & -\sin(\theta) \\ \sin(\theta) & \cos(\theta) \end{bmatrix} \begin{bmatrix} q_{nx_0}^{(2)}(x_0, y_0) \\ q_{ny_0}^{(2)}(x_0, y_0) \end{bmatrix}, \tag{4.1.10}$$

$$\begin{bmatrix} u_n^{tot}(x,y) \\ v_n^{tot}(x,y) \end{bmatrix} = \begin{bmatrix} u_n^{(1)}(x,y) \\ v_n^{(1)}(x,y) \end{bmatrix} + \begin{bmatrix} \cos(\theta) & -\sin(\theta) \\ \sin(\theta) & \cos(\theta) \end{bmatrix} \begin{bmatrix} u_n^{(2)}(x_0,y_0) \\ v_n^{(2)}(x_0,y_0) \end{bmatrix}, \tag{4.1.11}$$

$$\begin{bmatrix} \sigma_{nxx}^{tot}(x,y) \\ \sigma_{nxy}^{tot}(x,y) \\ \sigma_{nyy}^{tot}(x,y) \end{bmatrix} = \begin{bmatrix} \cos^2(\theta) & \sin^2(\theta) & -\sin(2\theta) \\ \frac{\sin(2\theta)}{2} & -\frac{\sin(2\theta)}{2} & \cos(2\theta) \\ \sin^2(\theta) & \cos^2(\theta) & \sin(2\theta) \end{bmatrix} \begin{bmatrix} \sigma_{nx_0x_0}^{(2)}(x_0,y_0) \\ \sigma_{ny_0y_0}^{(2)}(x_0,y_0) \\ \sigma_{nx_0y_0}^{(2)}(x_0,y_0) \end{bmatrix} + \begin{bmatrix} \sigma_{nxx}^{(1)}(x,y) \\ \sigma_{nxy}^{(1)}(x,y) \\ \sigma_{nyy}^{(1)}(x,y) \end{bmatrix}, \tag{4.1.12}$$

and those can be determined in the $x_0o_0y_0$ coordinate system by

$$T_n^{tot}(x_0,y_0) = T_n^{(1)}(x,y) + T_n^{(2)}(x_0,y_0), \tag{4.1.13}$$

$$\begin{bmatrix} q_{nx_0}^{tot}(x_0,y_0) \\ q_{ny_0}^{tot}(x_0,y_0) \end{bmatrix} = \begin{bmatrix} \cos(\theta) & \sin(\theta) \\ -\sin(\theta) & \cos(\theta) \end{bmatrix} \begin{bmatrix} q_{nx}^{(1)}(x,y) \\ q_{ny}^{(1)}(x,y) \end{bmatrix} + \begin{bmatrix} q_{nx_0}^{(2)}(x_0,y_0) \\ q_{nxy_0}^{(2)}(x_0,y_0) \end{bmatrix}, \tag{4.1.14}$$

$$\begin{bmatrix} u_n^{tot}(x_0,y_0) \\ v_n^{tot}(x_0,y_0) \end{bmatrix} = \begin{bmatrix} u_n^{(1)}(x_0,y_0) \\ v_n^{(1)}(x,y) \end{bmatrix} + \begin{bmatrix} \cos(\theta) & -\sin(\theta) \\ \sin(\theta) & \cos(\theta) \end{bmatrix} \begin{bmatrix} u_n^{(2)}(x_0,y_0) \\ v_n^{(2)}(x_0,y_0) \end{bmatrix}, \tag{4.1.15}$$

$$\begin{bmatrix} \sigma_{nx_0x_0}^{tot}(x_0,y_0) \\ \sigma_{nx_0y_0}^{tot}(x_0,y_0) \\ \sigma_{ny_0y_0}^{tot}(x_0,y_0) \end{bmatrix} = \begin{bmatrix} \cos^2(\theta) & \sin^2(\theta) & \sin(2\theta) \\ -\frac{\sin(2\theta)}{2} & \frac{\sin(2\theta)}{2} & \cos(2\theta) \\ \sin^2(\theta) & \cos^2(\theta) & -\sin(2\theta) \end{bmatrix} \begin{bmatrix} \sigma_{nxx}^{(1)}(x,y) \\ \sigma_{nyy}^{(1)}(x,y) \\ \sigma_{nxy}^{(1)}(x,y) \end{bmatrix} + \begin{bmatrix} \sigma_{nx_0x_0}^{(2)}(x_0,y_0) \\ \sigma_{nx_0y_0}^{(2)}(x_0,y_0) \\ \sigma_{ny_0y_0}^{(2)}(x_0,y_0) \end{bmatrix}. \tag{4.1.16}$$

The governing equation of heat conduction and corresponding boundary-continuity conditions are as follows

$$\frac{\partial}{\partial x'} q'_{nx'}(x',y') + \frac{\partial}{\partial y'} q'_{ny'}(x',y') = 0, \tag{4.1.17}$$

$$q_{1x}^{tot}(0,y) = Q_0, \qquad q_{2x}^{tot}(h_1+h_2,y) = Q_0, \qquad -\infty < y < \infty \tag{4.1.18}$$

$$T_1^{tot}(h_1,y) = T_2^{tot}(h_1,y), \qquad q_{1x}^{tot}(h_1,y) = q_{2x}^{tot}(h_1,y), \qquad -\infty < y < \infty \tag{4.1.19}$$

$$q_{ny_0}^{tot}(x_0,0^+) = q_{ny_0}^{tot}(x_0,0^-) = -k_n^* Q_0 \sin(\theta), \qquad a_0 < x_0 < b_0, \tag{4.1.20}$$

where $q'_{nx'} = -k'_n \ \partial T'_n/\partial x', q'_{ny'} = -k'_n \ \partial T'_n/\partial y'$, Q_0 is the heat flux corresponding to perfect conduction case and k^* is a heat conductivity index which vary between 0 to 1. $k^* = 0, 1$ correspond to perfect insulation and perfect conduction along the crack surfaces. The notations having superscript ($'$) will reduce to the variables depending on states e.g., in the second state $q'_n(x', y')$ is converted to $q_n^{(2)}(x_0, y_0)$ and similarly for other notations. Equation (4.1.18) shows that heat flow is applied along the x-direction to the strip's top surface (I) and bottom surface (II), respectively. The temperature and heat flux continuity conditions at the interface are represented by equation (4.1.19). The equation (4.1.20) represents the partial insulation of the crack surfaces under the assumption that the crack allows some heat flux Q^* which is only a certain percentage of the heat flux corresponding to the perfect conduction case. Given below are the plane elasticity equation and corresponding boundary-continuity conditions:

$$\frac{\partial}{\partial x'}\sigma'_{nx'x'}(x', y') + \frac{\partial}{\partial y'}\sigma'_{nx'y'}(x', y') = 0, \tag{4.1.21}$$

$$\frac{\partial}{\partial x'}\sigma'_{nx'y'}(x', y') + \frac{\partial}{\partial y'}\sigma'_{ny'y'}(x', y') = 0, \tag{4.1.22}$$

$$\sigma^{tot}_{1xx}(0, y) = 0, \qquad \sigma^{tot}_{1xy}(0, y) = 0, \qquad -\infty < y < \infty \tag{4.1.23}$$

$$\sigma^{tot}_{2xx}(h_1 + h_2, y) = 0, \qquad \sigma^{tot}_{2xy}(h_1 + h_2, y) = 0, \qquad -\infty < y < \infty \tag{4.1.24}$$

$$\sigma^{tot}_{1xx}(h_1, y) = \sigma^{tot}_{2xx}(h_1, y), \qquad \sigma^{tot}_{1xy}(h_1, y) = \sigma^{tot}_{2xy}(h_1, y), \qquad -\infty < y < \infty \tag{4.1.25}$$

$$u^{tot}_1(h_1, y) = u^{tot}_2(h_1, y), \qquad v^{tot}_1(h_1, y) = v^{tot}_2(h_1, y), \qquad -\infty < y < \infty \tag{4.1.26}$$

$$\sigma^{tot}_{ny_0y_0}(x_0, 0^+) = \sigma^{tot}_{ny_0y_0}(x_0, 0^-) = p_1(x_0), \qquad a_0 < x_0 < b_0, \tag{4.1.27}$$

$$\sigma^{tot}_{nx_0y_0}(x_0, 0^+) = \sigma^{tot}_{nx_0y_0}(x_0, 0^-) = p_2(x_0), \qquad a_0 < x_0 < b_0, \tag{4.1.28}$$

where equations (4.1.23) and (4.1.24) show that the top surface of the strip (I) and bottom surface of the strip (II) are stress-free. The stress and displacement continuity conditions at the interface are represented by equations (4.1.25) and (4.1.26),

respectively. The mechanical loading conditions which have been applied to the crack faces are shown by equations (4.1.27) and (4.1.28). Hooke's law is used to determine the relationship between displacement and stress components [102].

4.1.3 Solution of temperature field

4.1.3.1 Temperature field of the first state

Writing equation (4.1.17) for the considered uncracked composite structure and applying Fourier transforms in y, the temperature field for the first state is expressed as

$$T_n^{(1)}(x,y) = \frac{1}{2\pi}\int_{-\infty}^{\infty}\sum_{j=1}^{2} G_{nj}^{(1)}(\alpha)e^{\lambda_{nj}^{(1)}(\alpha)x - i\alpha y}d\alpha, \tag{4.1.29}$$

where α is the variable related to Fourier transform, $G_{nj}^{(1)}(\alpha)$ are unknown functions in α and $\lambda_{nj}^{(1)}(\alpha)$ $(n = 1, 2; j = 1, 2)$ are determined by

$$\lambda_{nj}^{(1)}(\alpha) = \frac{-\delta_n + (-1)^j\sqrt{\delta_n^2 + 4\alpha^2}}{2}. \tag{4.1.30}$$

4.1.3.2 Temperature field of the second state

Writing equation (4.1.17) for the considered cracked composite structure and using Fourier transforms in x_0, the expressions of temperature field above and below the cracks' region are expressed as

$$T_n^{(2)}(x_0,y_0) = \begin{cases} \frac{1}{2\pi}\int_{-\infty}^{\infty}\sum_{j=1}^{2} G_{nj}^{(2)}(s)e^{\lambda_{nj}^{(2)}(s)y_0 - isx_0}ds, & y_0 > 0, \\ \frac{1}{2\pi}\int_{-\infty}^{\infty}\sum_{j=1}^{2} G_{nj+2}^{(2)}(s)e^{\lambda_{nj}^{(2)}(s)y_0 - isx_0}ds, & y_0 < 0, \end{cases} \tag{4.1.31}$$

where s is the Fourier transformed variable, $G_{nj}^{(2)}(s)$ are unknown functions of s and $\lambda_{nj}^{(2)}(s)$ $(n=1,2;j=1,2)$ are given by

$$\lambda_{nj}^{(2)}(s)=\frac{-\delta_{n2}+(-1)^j\sqrt{\delta_{n2}^2+4(s^2+is\delta_{n1})}}{2}. \tag{4.1.32}$$

The regularity condition [37] give $G_{n2}^{(2)}(s)=0$ and $G_{n3}^{(2)}(s)=0$. Expressing the jump of temperature across crack surfaces by

$$\phi(x_0)=T_n^{(2)}(x_0,0^+)-T_n^{(2)}(x_0,0^-),\qquad n=1,2, \tag{4.1.33}$$

and the application of inverse Fourier transform and continuity conditions at $y_0=0$ give

$$\begin{aligned} &G_{n1}^{(2)}(s)=W_{n1}^{(2)}(s)\Phi(s),\quad G_{n4}^{(2)}(s)=W_{n2}^{(2)}(s)\Phi(s), \\ \text{where}\quad &W_{n1}^{(2)}(s)=\frac{\lambda_{n2}^{(2)}(s)}{\lambda_{n2}^{(2)}(s)-\lambda_{n1}^{(2)}(s)},\ W_{n2}^{(2)}(s)=\frac{\lambda_{n1}^{(2)}(s)}{\lambda_{n2}^{(2)}(s)-\lambda_{n1}^{(2)}(s)}, \\ &\Phi(s)=\int_{-\infty}^{\infty}\phi(x_0)e^{isx_0}dx_0. \end{aligned} \tag{4.1.34}$$

4.1.3.3 Numerical solution of integral equation related to temperature field

The boundary continuity conditions (4.1.18) and (4.1.19) are used to find the remaining unknowns obtained in the first and second states as well as the total temperature field in the xoy coordinate system. These conditions give the following four equations as

$$\sum_{j=1}^{2}G_{nj}^{(1)}(\alpha)\lambda_{nj}^{(1)}(\alpha)e^{\lambda_{nj}^{(1)}(\alpha)x_n}=-\frac{Q_0\overline{\delta(\alpha)}}{k_n(x_n)}+\frac{1}{2\pi}\int_{-\infty}^{\infty}\sum_{j=1}^{2}G_{nj}^{(2)}(s)F_{tnj}^{(2)}(s)I_{tnj}(s,\alpha,x_n)$$

$$\times \Phi(s)ds, \qquad n = 1, 2,$$

$$\sum_{j=1}^{2}\sum_{n=1}^{2}(-1)^n G_{nj}^{(1)}(\alpha)e^{\lambda_{nj}^{(1)}(\alpha)h_1} = \frac{1}{2\pi}\int_{-\infty}^{\infty}\sum_{j=1}^{2}\sum_{n=1}^{2}(-1)^{n+1}G_{nj}^{(2)}(s)I_{tnj}(s,\alpha,h_1)\Phi(s)ds,$$

$$\sum_{j=1}^{2}\sum_{n=1}^{2}(-1)^n k_n(h_1)G_{nj}^{(1)}(\alpha)\lambda_{nj}^{(1)}(\alpha)e^{\lambda_{nj}^{(1)}(\alpha)h_1} = \frac{1}{2\pi}\int_{-\infty}^{\infty}\sum_{j=1}^{2}\sum_{n=1}^{2}(-1)^n k_n(h_1)G_{nj}^{(2)}(s)F_{tnj}^{(2)}(s)$$

$$\times I_{tnj}(s,\alpha,h_1)\Phi(s)ds,$$

where $x_1 = 0, x_2 = h_1 + h_2$. $F_{tnj}^{(2)}(s)$ and $I_{tij}(s,\alpha,x)$ are mentioned in Appendix C. Utilizing the above four equations, the unknown $G_{nj}^{(1)}(\alpha)$ can be written in matrix form as

$$\begin{bmatrix} G_{11}^{(1)}(\alpha) \\ G_{12}^{(1)}(\alpha) \\ G_{21}^{(1)}(\alpha) \\ G_{22}^{(1)}(\alpha) \end{bmatrix} = \frac{Q_0}{k_{01}}\begin{bmatrix} G_{111}^{(1)}(\alpha) \\ G_{112}^{(1)}(\alpha) \\ G_{121}^{(1)}(\alpha) \\ G_{122}^{(1)}(\alpha) \end{bmatrix} + \frac{1}{2\pi}\int_{-\infty}^{\infty}\begin{bmatrix} G_{211}(\alpha,s) \\ G_{212}(\alpha,s) \\ G_{221}(\alpha,s) \\ G_{222}(\alpha,s) \end{bmatrix}\Phi(s)\,ds. \tag{4.1.35}$$

The condition (4.1.20) gives the following singular integral equation as

$$\int_{-\infty}^{\infty} N_n(s,x_0)\,\Phi(s)ds = \frac{k_n^* Q_0\sin(\theta)}{k_n(x_0,0^+)} + \frac{Q_0 S_n(x_0)}{k_{01}}, \qquad a_0 < x_0 < b_0, \tag{4.1.36}$$

where $N_n(s,x_0)$ and $S_n(x_0)$ are given in equations (C.0.4)-(C.0.5). Expressing the jump of temperature $\phi(x_0)$ as a series of Jacobi polynomial as

$$\phi(x_0) = \begin{cases} \sum_{k=0}^{\infty} a_{0k}\frac{Q_0}{k_{01}}\,P_k^{\left(\frac{1}{2},\frac{1}{2}\right)}(j_0)\,(1-j_0^2)^{\frac{1}{2}}, & a_0 \le x_0 \le b_0, \\ 0, & x_0 < a_0,\ b_0 < x_0, \end{cases} \tag{4.1.37}$$

where $j_0 = \left(x_0 - \frac{a_0+b_0}{2}\right)/\left(\frac{b_0-a_0}{2}\right)$. The Fourier transform of equation (4.1.37) gives

$$\Phi(s)=\sum_{k=0}^{\infty}\frac{a_{0k}B_kG_kQ_0}{k_{01}s}J_{k+1}\left(s\frac{b_0-a_0}{2}\right), \tag{4.1.38}$$

where $B_k=\frac{\Gamma\left(k+1+\frac{1}{2}\right)}{k!}$, $G_k=2\sqrt{\pi}(-1)^n i^n$ with Γ, J_k are the Gamma and Bessel functions, respectively and a_{0k} are the unknowns to be determined by using the Schmidt method [77, 121].

4.1.4 Solution of stress field

4.1.4.1 Stress field of the first state

Solving equations (4.1.21) and (4.1.22) for the first state and applying Fourier transform in y, the expressions of displacement components for the first state are given by

$$u_n^{(1)}(x,y)=\frac{1}{2\pi}\int_{-\infty}^{\infty}\left(\sum_{j=1}^{4}A_{nj}^{(1)}(\alpha)E_{nj}^{(1)}(\alpha)e^{\tau_{nj}^{(1)}(\alpha)x}+4\alpha_n(x)\sum_{j=1}^{2}\frac{\eta_{nj}^{(1)}(\alpha)}{d_{nj}^{(1)}(\alpha)}G_{nj}^{(1)}(\alpha)e^{\lambda_{nj}^{(1)}(\alpha)x}\right)e^{-i\alpha y}d\alpha,$$
$$v_n^{(1)}(x,y)=\frac{1}{2\pi}\int_{-\infty}^{\infty}\left(\sum_{j=1}^{4}A_{nj}^{(1)}(\alpha)e^{\tau_{nj}^{(1)}(\alpha)x}+4\alpha_n(x)\sum_{j=1}^{2}\frac{\zeta_{nj}^{(1)}(\alpha)}{d_{nj}^{(1)}(\alpha)}G_{nj}^{(1)}(\alpha)e^{\lambda_{nj}^{(1)}(\alpha)x}\right)e^{-i\alpha y}d\alpha,$$

where α is the Fourier variable, $A_{nj}^{(1)}(\alpha)$ are unknown functions in α to be determined, $E_{nj}^{(1)}(\alpha)$, $\eta_{nj}^{(1)}(\alpha),\zeta_{nj}^{(1)}(\alpha),d_{nj}^{(1)}(\alpha)$ are known functions given by equations (C.0.6)-(C.0.9) of Appendix C and $\tau_{nj}^{(1)}(\alpha)$ $(n=1,2;j=1,2,...,4)$ are given by

$$\tau_{nj}^{(1)}(\alpha)=\frac{1}{2}\left(-\beta_n+(-1)^j\sqrt{4\alpha^2+\beta_n^2-4if_0\alpha\beta_n}\right),\ \tau_{n2}^{(1)}(\alpha)=\overline{\tau_{n1}^{(1)}(\alpha)},\ \tau_{n3}^{(1)}(\alpha)=\overline{\tau_{n4}^{(1)}(\alpha)}, \tag{4.1.39}$$

where $n = 1, 2;\ j = 1, 4,\ f_0 = \sqrt{(3-k)/(1+k)}$ and $k = 3 - 4\nu, (3-4\nu)/(1+\nu)$ for plane strain and plane stress, respectively.

4.1.4.2 Stress field of the second state

Writing the equations (4.1.21) and (4.1.22) for the second state and applying Fourier transforms in x_0, the expression of the displacement field above and below the cracks' region are

$$u_n^{(2)}(x_0, y_0) = \begin{cases} \frac{1}{2\pi}\int_{-\infty}^{\infty} \left[\sum_{j=1}^{4} A_{nj}^{(2)}(s) E_{nj}^{(2)}(s) e^{\tau_{nj}^{(2)}(s) y_0} \right. \\ \left. + \frac{4\alpha_n(x_0,y_0)\eta_{n1}^{(2)}(s)}{d_{n1}^{(2)}(s)} G_{n1}^{(2)}(s) e^{\lambda_{n1}^{(2)}(s) y_0} \right] e^{-isx_0} ds, \quad y_0 > 0, \\ \frac{1}{2\pi}\int_{-\infty}^{\infty} \left[\sum_{j=1}^{4} A_{nj+4}^{(2)}(s) E_{nj}^{(2)}(s) e^{\tau_{nj}^{(2)}(s) y_0} \right. \\ \left. + \frac{4\alpha_n(x_0,y_0)\eta_{n2}^{(2)}(s)}{d_{n2}^{(2)}(s)} G_{n4}^{(2)}(s) e^{\lambda_{n2}^{(2)}(s) y_0} \right] e^{-isx_0} ds, \quad y_0 < 0, \end{cases} \tag{4.1.40}$$

$$v_n^{(2)}(x_0, y_0) = \begin{cases} \frac{1}{2\pi}\int_{-\infty}^{\infty} \left[\sum_{j=1}^{4} A_{nj}^{(2)}(s) e^{\tau_{nj}^{(2)}(s) y_0} \right. \\ \left. + \frac{4\alpha_n(x_0,y_0)\zeta_{n1}^{(2)}(s)}{d_{n1}^{(2)}(s)} G_{n1}^{(2)}(s) e^{\lambda_{n1}^{(2)}(s) y_0} \right] e^{-isx_0} ds, \quad y_0 > 0, \\ \frac{1}{2\pi}\int_{-\infty}^{\infty} \left[\sum_{j=1}^{4} A_{nj+4}^{(2)}(s) e^{\tau_{nj}^{(2)}(s) y_0} \right. \\ \left. + \frac{4\alpha_n(x_0,y_0)\zeta_{n2}^{(2)}(s)}{d_{n2}^{(2)}(s)} G_{n4}^{(2)}(s) e^{\lambda_{n2}^{(2)}(s) y_0} \right] e^{-isx_0} ds, \quad y_0 < 0, \end{cases} \tag{4.1.41}$$

where $A_{nj}^{(2)}(s)$ are unknown functions in s to be determined, $E_{nj}^{(2)}(s)$, $\eta_{nj}^{(2)}(s)$, $\zeta_{nj}^{(2)}(s)$, $d_{nj}^{(2)}(s)$ are known functions of s given in Appendix C and $\tau_{nj}^{(2)}(s)$ $(n = 1, 2; j = 1, 2, 3, 4)$ are determined by

$$\tau_{nj}^{(2)} = \frac{1}{2}\left[e_{0j}\sqrt{\left(\beta_{n2} + (-1)^{j+1} f_0 \beta_{n1}\right)^2 + 4s\left(s + i\beta_{n1} + (-1)^j i f_0 \beta n2\right)} - \beta_{n2} + (-1)^j f_0 \beta_{n1} \right], \tag{4.1.42}$$

where $e_{0j} = (-1)$ for $j = 1, 2$ and $e_{0j} = 1$ for $j = 3, 4$. Regularity conditions [37, 102] give $A^{(2)}_{nj}(s) = 0$, $j = 3, 4, 5, 6$. Expressing the jump of the displacements as

$$\psi_1(x_0) = u^{(2)}_n(x_0, 0^+) - u^{(2)}_n(x_0, 0^-),\ \psi_2(x_0) = v^{(2)}_n(x_0, 0^+) - v^{(2)}_n(x_0, 0^-), \quad (4.1.43)$$

and stress continuity conditions at $y_0 = 0$ give

$$\sum_{j=1}^{2} X^{(2)}_{knj}(s)A^{(2)}_{nj}(s) + \alpha_{01}X^{(2)}_{tkn1}(s) = \sum_{j=3}^{4} X^{(2)}_{knj}(s)A^{(2)}_{nj+4}(s) + \alpha_{01}X^{(2)}_{tkn2}(s),\ \ k = 1, 2,$$
$$\sum_{j=1}^{2} X^{(2)}_{knj}(s)A^{(2)}_{nj}(s) + \alpha_{01}X^{(2)}_{tkn1}(s) = \Psi_{k-2}(s) + \sum_{j=3}^{4} X^{(2)}_{knj}(s)A^{(2)}_{nj+4}(s) + \alpha_{01}X^{(2)}_{tkn2}(s),\ k = 3, 4,$$

which can be rewritten as

$$A^{(2)}_{nj}(s) = \alpha_{01}A^{(2)}_{1nj}(s) + A^{(2)}_{2nj}(s)\Psi_1(s) + A^{(2)}_{3nj}(s)\Psi_2(s), \quad (4.1.44)$$

where $X^{(2)}_{knj}(s)$, $X^{(2)}_{tknj}(s)$ are given by equation (C.0.21) and $\Psi_k(s) = \int_{-\infty}^{\infty} \psi_k(x_0)e^{isx_0}dx_0$.

4.1.4.3 Numerical solution of integral equations related to stress field

The boundary continuity conditions (4.1.23)-(4.1.26) are used to calculate the unknowns obtained in the first and second states as well as the total stress field in the xoy coordinate system and give the following equations:

$$\sum_{j=1}^{4}\left[A^{(1)}_{nj}(\alpha)\Gamma^{(1)}_{knj}(\alpha, x_n) + \frac{1}{2\pi}\int_{-\infty}^{\infty} A^{(2)}_{nj}(s)L^{(2)}_{knj}(s)I_{nj}(s, \alpha, x_n)ds\right]$$
$$= -\alpha_{01}\sum_{j=1}^{2}\left[\Gamma^{(1)}_{tknj}(\alpha, x_n) + \frac{1}{2\pi}\int_{-\infty}^{\infty}\left[L^{(2)}_{tknj}(s)I_{tnj}(s, \alpha, x_n)ds\right], \qquad k = 1, 2; n = 1, 2,$$
$$\sum_{n=1}^{2}\sum_{j=1}^{4}(-1)^{n+1}\left[\mu_n(h_1)A^{(1)}_{nj}(\alpha)\Gamma^{(1)}_{knj}(\alpha, h_1) + \frac{1}{2\pi}\int_{-\infty}^{\infty} A^{(2)}_{nj}(s)L^{(2)}_{knj}(s)I_{nj}(s, \alpha, h_1)ds\right]$$

$$= \alpha_{01} \sum_{n=1}^{2} \sum_{j=1}^{2} (-1)^n \left[\mu_n(h_1) \Gamma^{(1)}_{tk1j}(\alpha, h_1) + \frac{1}{2\pi} \int_{-\infty}^{\infty} L^{(2)}_{tknj}(s) I_{tnj}(s, \alpha, h_1) ds \right], \; k = 1, 2, 3, 4,$$

where $\Gamma^{(1)}_{knj}(\alpha, x_n)$, $\Gamma^{(1)}_{tknj}(\alpha, x_n)$, $L^{(2)}_{knj}(s)$, $L^{(2)}_{tknj}(s)$ and $I_{nj}(s, \alpha, x)$ are given in Appendix C. $A^{(1)}_{nj}(\alpha)$ can be expressed in terms of $\Psi_1(s)$ and $\Psi_2(s)$ utilizing equation (4.1.44) and above equations as

$$\begin{bmatrix} A^{(1)}_{11}(\alpha) \\ A^{(1)}_{12}(\alpha) \\ A^{(1)}_{21}(\alpha) \\ A^{(1)}_{22}(\alpha) \end{bmatrix} = \alpha_{01} \begin{bmatrix} A^{(1)}_{111}(\alpha) \\ A^{(1)}_{112}(\alpha) \\ A^{(1)}_{121}(\alpha) \\ A^{(1)}_{122}(\alpha) \end{bmatrix} + \frac{1}{2\pi} \int_{-\infty}^{\infty} \left\{ \alpha_{01} \begin{bmatrix} A_{211}(\alpha, s) \\ A_{212}(\alpha, s) \\ A_{221}(\alpha, s) \\ A_{222}(\alpha, s) \end{bmatrix} \Phi(s) + \begin{bmatrix} A_{311}(\alpha, s) \\ A_{312}(\alpha, s) \\ A_{321}(\alpha, s) \\ A_{322}(\alpha, s) \end{bmatrix} \Psi_1(s) + \begin{bmatrix} A_{411}(\alpha, s) \\ A_{412}(\alpha, s) \\ A_{421}(\alpha, s) \\ A_{422}(\alpha, s) \end{bmatrix} \Psi_2(s) \right\} ds.$$

The following singular integral equations are obtained with the help of conditions (4.1.27) and (4.1.28) as

$$\int_{-\infty}^{\infty} (M_{n11}(s, x_0)\Psi_1(s) + M_{n12}(s, x_0)\Psi_2(s)) ds = \frac{2\pi p_1(x_0)}{\mu_n(x_0, 0^+)} + \alpha_{01} \left[R_{n1}(x_0) + R_{tn1}(x_0) \right], \quad a_0 < x_0 < b_0, \tag{4.1.45}$$

$$\int_{-\infty}^{\infty} (M_{n21}(s, x_0)\Psi_1(s) + M_{n22}(s, x_0)\Psi_2(s)) ds = \frac{2\pi p_2(x_0)}{\mu_n(x_0, 0^+)} + \alpha_{01} \left[R_{n2}(x_0) + R_{tn2}(x_0) \right], \quad a_0 < x_0 < b_0, \tag{4.1.46}$$

where $M_{njk}(s, x_0)$, $R_{nj}(x_0)$ and $R_{tnj}(x_0)$ are mentioned in equations (C.0.33)-(C.0.35) given in Appendix C. The residue theory is used to solve the above integral equations. The unknown functions ψ_i can be expressed as

$$\psi_1(x_0) = \begin{cases} \sum_{k=0}^{\infty} b_{0k}\, P_k^{\left(\frac{1}{2},\frac{1}{2}\right)}(j_0)\,(1-j_0^2)^{\frac{1}{2}}, & a_0 \le x_0 \le b_0, \\ 0, & x_0 < a_0,\ b_0 < x_0, \end{cases} \tag{4.1.47}$$

$$\psi_2(x_0) = \begin{cases} \sum_{k=0}^{\infty} c_{0k}\, P_k^{\left(\frac{1}{2},\frac{1}{2}\right)}(j_0)\,(1-j_0^2)^{\frac{1}{2}}, & a_0 \le x_0 \le b_0, \\ 0, & x_0 < a_0,\ b_0 < x_0, \end{cases} \tag{4.1.48}$$

where unknowns b_{0k} and c_{0k} are to be determined by using the Schmidt method [77, 121].

4.1.5 Driving force parameters

The mode I and mode II crack tip stress intensity factors (SIFs) are determined by

$$K_I^{a_0} = \lim_{x_0 \to a_0} \sqrt{2(a_0 - x_0)}\ \sigma_{ny_0y_0}^{tot}(x_0, 0), \tag{4.1.49}$$

$$K_I^{b_0} = \lim_{x_0 \to b_0} \sqrt{2(x_0 - b_0)}\ \sigma_{ny_0y_0}^{tot}(x_0, 0), \tag{4.1.50}$$

$$K_{II}^{a_0} = \lim_{x_0 \to a_0} \sqrt{2(a_0 - x_0)}\ \sigma_{nx_0y_0}^{tot}(x_0, 0), \tag{4.1.51}$$

$$K_{II}^{b_0} = \lim_{x_0 \to b_0} \sqrt{2(x_0 - b_0)}\ \sigma_{nx_0y_0}^{tot}(x_0, 0), \tag{4.1.52}$$

where $n = 1, 2$ represent strip (I) and strip (II), respectively.

In terms of unknowns b_{0k} and c_{0k}, the crack tip SIFs can be expressed as

$$K_I^{a_0} = \frac{-2\delta_2\mu_n(a_0, 0)}{\sqrt{\pi l}} \sum_{k=0}^{\infty} (-1)^k c_{0k} B_k, \tag{4.1.53}$$

$$K_I^{b_0} = \frac{-2\delta_2\mu_n(b_0, 0)}{\sqrt{\pi l}} \sum_{k=0}^{\infty} c_{0k} B_k, \tag{4.1.54}$$

$$K_{II}^{a_0} = \frac{-2\delta_3\mu_n(a_0, 0)}{\sqrt{\pi l}} \sum_{k=0}^{\infty} (-1)^k b_{0k} B_k, \tag{4.1.55}$$

$$K_{II}^{b_0} = \frac{-2\delta_3\mu_n(b_0,0)}{\sqrt{\pi l}} \sum_{k=0}^{\infty} b_{0k}B_k, \tag{4.1.56}$$

where $\delta_2 = \delta_3 = -2s/[(1+k)|s|]$ and $l = (b_0 - a_0)/2$.

In terms of SIFs and local material parametric function, the mode I and mode II crack tip strain energy release rates (SERRs) are evaluated by [98, 121]

$$G_I^{a_0} = \frac{\pi(k+1)}{8\mu_n(a_0,0)} (K_I^{a_0})^2, \tag{4.1.57}$$

$$G_I^{b_0} = \frac{\pi(k+1)}{8\mu_n(b_0,0)} (K_I^{b_0})^2, \tag{4.1.58}$$

$$G_{II}^{a_0} = \frac{\pi(k+1)}{8\mu_n(a_0,0)} (K_{II}^{a_0})^2, \tag{4.1.59}$$

$$G_{II}^{b_0} = \frac{\pi(k+1)}{8\mu_n(b_0,0)} (K_{II}^{b_0})^2. \tag{4.1.60}$$

4.1.6 Results and discussion

In this section of the chapter the influences of crack insulation, stiffness, heat conduction, thermal conductivity parameters, crack angle, and thickness of strips on normalized mode I and mode II crack tip SIFs and SERRs are obtained for an angled crack that goes from the strip (I) to strip (II) through the interface of functionally graded composite in the presence of thermo-mechanical loading. As the expression of SERR includes SIF and local material parametric function, so it contains more pertinent information as compared to SIF.

For computational purpose, uniform mechanical loadings on the crack faces are applied as $p_1(x_0) = -\sigma_0$ and $p_2(x_0) = -\sigma_0$ under the plane state condition. To normalize mode I and mode II stress intensity factors and strain energy release rates, the normalizing factors are chosen as $K_0 = \sqrt{l}(\sigma_0 + Q_0\alpha_{01}\mu_{01}l/k_{01})$ and $G_0 = \pi(k+1)K_0^2/(8\mu_{01})$, respectively. For simplicity, it is assumed that

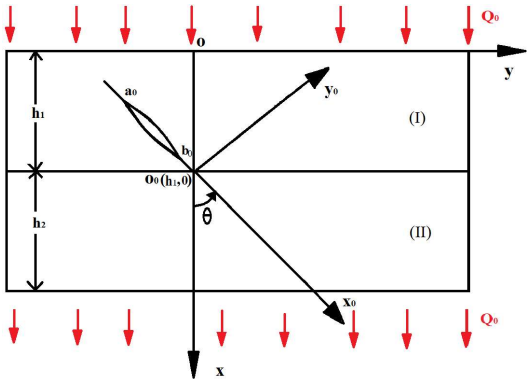

(a) $c_0/h_1 = -0.2,\ a_0/h_1 = -0.3,\ b_0/h_1 = -0.1.$

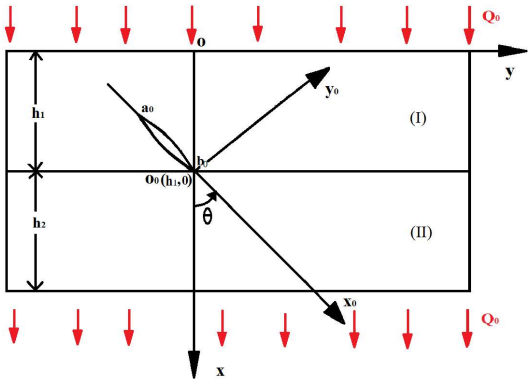

(b) $c_0/h_1 = -0.1,\ a_0/h_1 = -0.2,\ b_0/h_1 = 0.$

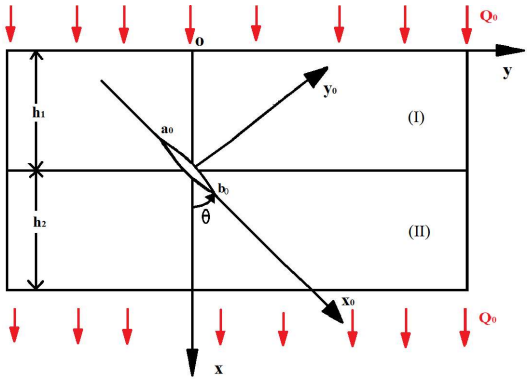

(c) $c_0/h_1 = 0,\ a_0/h_1 = -0.1,\ b_0/h_1 = 0.1.$

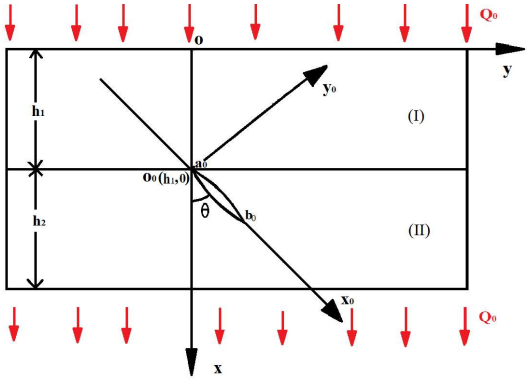

(d) $c_0/h_1 = 0.1,\ a_0/h_1 = 0,\ b_0/h_1 = 0.2.$

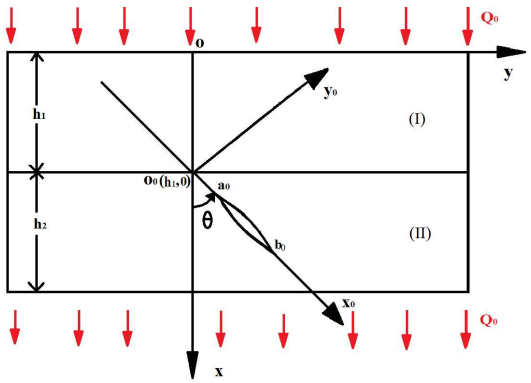

(e) $c_0/h_1 = 0.2,\ a_0/h_1 = 0.1,\ b_0/h_1 = 0.3.$

Figure 4.1.2: Schematics of the crack locations subjected to thermo - mechanical loading when the crack goes through the interface from the strip (I) to strip (II) for different values of normalized crack centre c_0/h_1 of the model under consideration.

$\nu = 0.3, (x_c, y_c) = (h_1, 0)$, normalized crack length $(b_0 - a_0)/h_1 = 0.2$, and c_0/h_1= normalized crack centre in x_0-direction i.e., $(b_0 + a_0)/(2h_1)$. Throughout the study c_0/h_1 ranges between -0.2 to 0.2. For the aforementioned values, Figure 4.1.2 demonstrates the schematic diagrams of the crack positions as the crack crosses the interface from strip (I) to strip (II) for different values of c_0/h_1. It is clear from the Figure 4.1.2 that for $c_0/h_1 = 0.1$, the crack tip a_0 passes through the interface whereas for $c_0/h_1 = -0.1$, the crack tip b_0 passes through the interface. Without loss of generality $k^* = 0.6, \theta = 54^o$, $h_1/h_2 = 1$, $\beta_1/\beta_2 = -1, \delta_1/\delta_2 = -1$, and $\gamma_1/\gamma_2 = -1$ are chosen. Even if one of those varies then the remaining parameters will have the mentioned values.

4.1.6.1 Validation

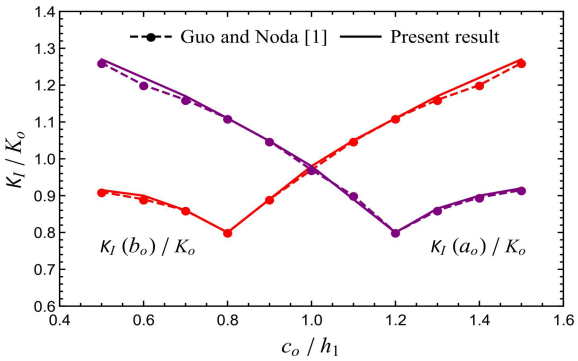

Figure 4.1.3: Comparison between obtained and existing outcomes [47] of normalized mode I crack tip SIFs as a function of normalized crack centre c_0/h_1 for a vertical crack that crosses the interface of bonded FGM strips.

For validation purpose, some results obtained by the present method are compared with the results given in [47], where the fracture problem of a vertical crack crossing the interface of functionally graded layered structure has been studied for mechanical loading. The present thermo-mechanical study can be reduced to the mechanical one by removing the terms corresponding to temperature. For $(x_c, y_c) =$

$(0,0)$, $\theta = 0^o$, $h_1/h_2 = 1$, $\beta_1/\beta_2 = -1$, $p_1(x_0) = -\sigma_0$, $p_2(x_0) = 0$ and normalizing factor for SIFs as $K_0 = \sigma_0\sqrt{(b_0 - a_0)/2}$, Figure 4.1.3 shows that the two studies coincide well.

4.1.6.2 Effect of crack insulation parameter

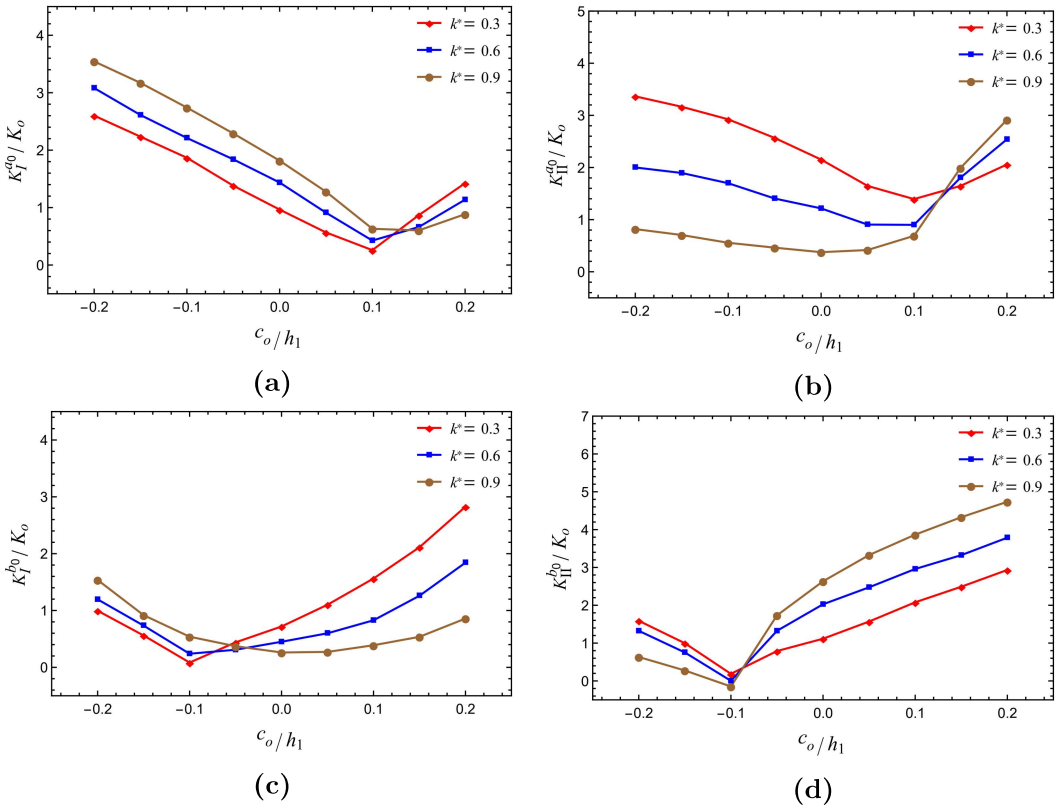

Figure 4.1.4: Variations in normalized mode I and mode II crack tip SIFs as a function of normalized crack centre c_0/h_1 for different values of crack insulation parameter k^*.

In the Figures 4.1.4 and 4.1.5, the impact of crack insulation parameter k^* on driving force parameters are illustrated. For $k^* = 0.3, 0.6, 0.9$, it can be observed from the Figures 4.1.4a and 4.1.4b that as the crack tip a_0 goes from the strip (I) to strip (II), the normalized mode I and mode II SIFs at the crack tip a_0 decrease and as it crosses the interface ($c_0/h_1 = 0.1$) and propagating further in the strip (II),

those are increased. Similar behavior is observed from Figures 4.1.4c and 4.1.4d for normalized mode I and mode II SIFs at the crack tip b_0 when crack tip b_0 goes from strip (I) to strip (II) crossing the interface ($c_0/h_1 = -0.1$).

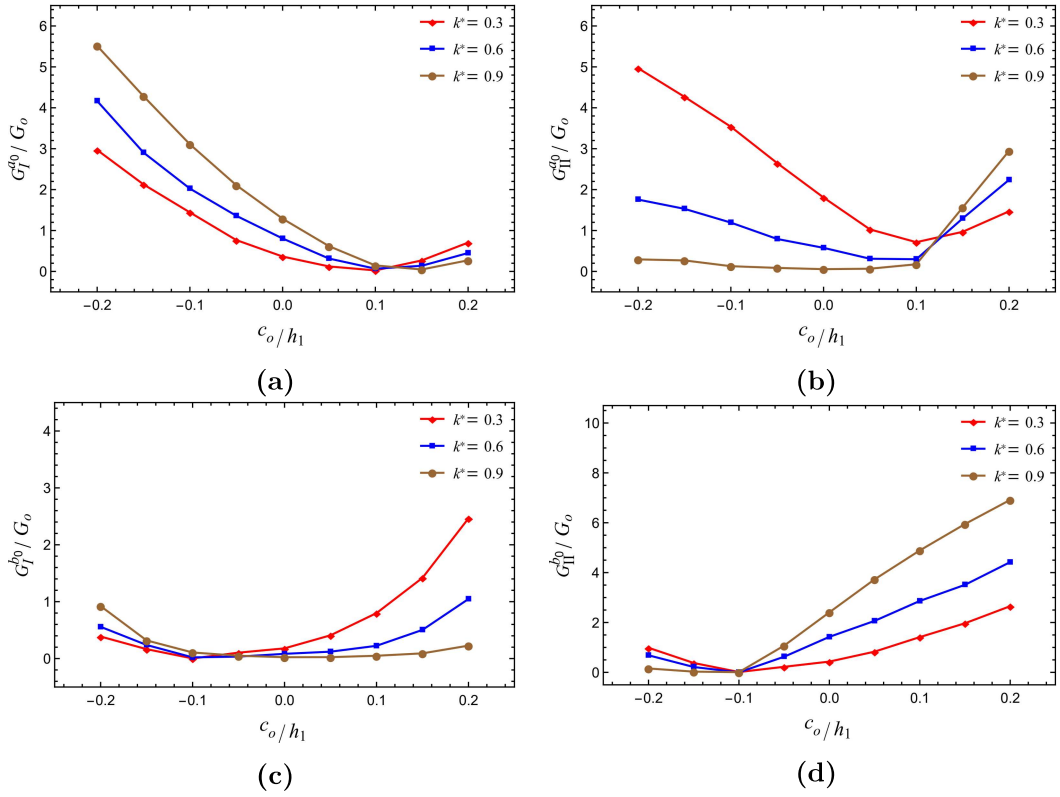

Figure 4.1.5: Variations in normalized mode I and mode II crack tip SERRs as a function of normalized crack centre c_0/h_1 for different values of crack insulation parameter k^*.

Further it can be concluded from Figures 4.1.4a and 4.1.4c that for $k^* = 0.3, 0.6, 0.9$, i.e., as k^* increases, the normalized mode I crack tip SIFs increase in strip (I) but as the crack tip reaches the strip (II) those decrease for increasing values of k^*. Whereas opposite nature is observed for normalized mode II crack tip SIFs as shown from the Figures 4.1.4b and 4.1.4d, i.e., in the strip (I) as k^* increases the normalized mode II crack tip SIFs decrease but in the strip (II) those increase with

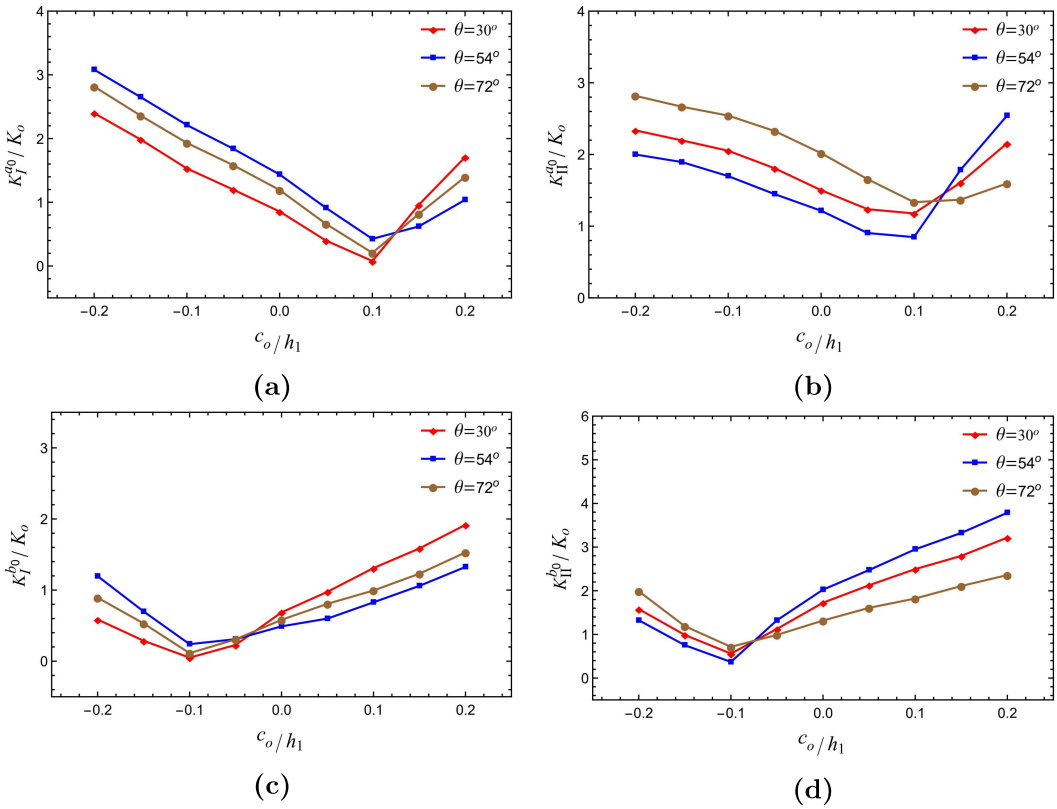

Figure 4.1.6: Variations in normalized mode I and mode II crack tip SIFs as a function of normalized crack centre c_0/h_1 for different values of crack orientation angle θ.

k^*. Due to the non-homogeneity of the FGM strips and applied mechanical loading the said opposite natures are observed.

It is clear from Figure 4.1.5 that a similar impact of k^* on normalized mode I and mode II SERRs are obtained when the crack goes through the interface. In other words as the insulating nature of the crack surface decreases, the magnitudes of driving force parameters viz. SIFs and SERRs increase in the strip (I) while those decrease in the strip (II). The reverse nature are found for mode II SIFs and SERRs.

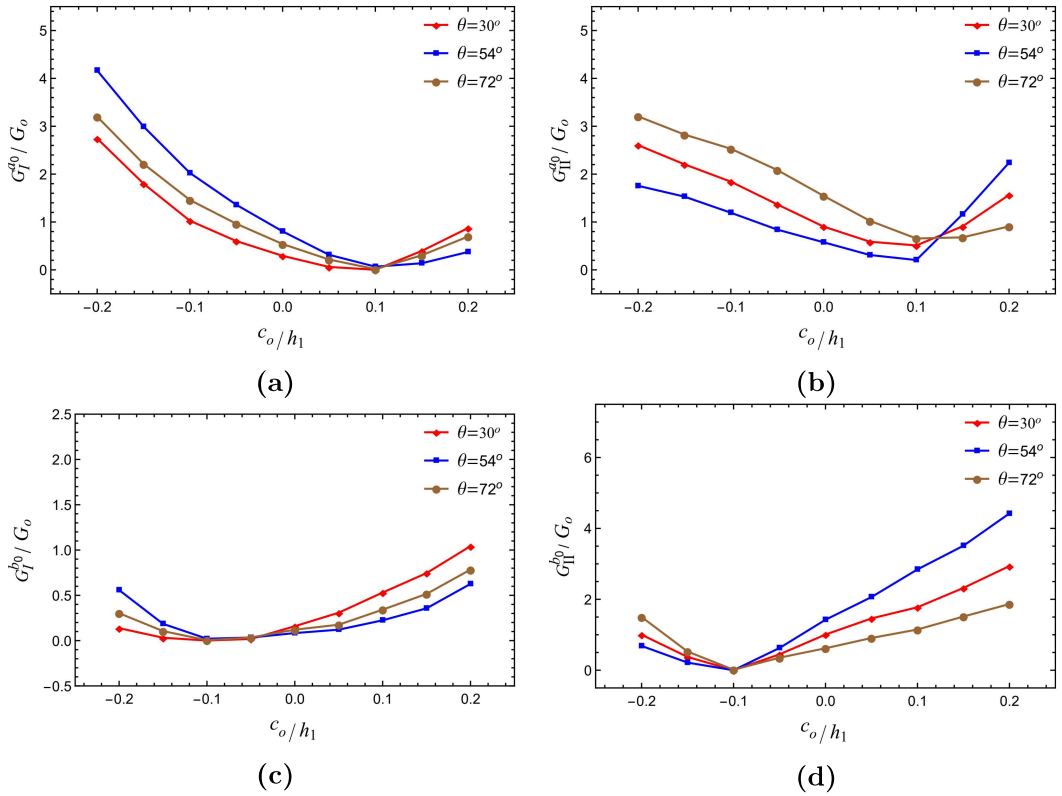

Figure 4.1.7: Variations in normalized mode I and mode II crack tip SERRs as a function of normalized crack centre c_0/h_1 for different values of crack orientation angle θ.

4.1.6.3 Effect of crack orientation angle

The influence of crack orientation angle θ on the driving force parameters SIFs and SERRs are presented in Figures 4.1.6 and 4.1.7 which illustrate that in this case as the crack tips a_0 and b_0 reach the interface for $c_0/h_1 = 0.1$ and -0.1, respectively of the considered composite structure under thermo-mechanical loading. The magnitudes of normalized mode I and mode II driving force parameters initially decrease and after crossing the interface those are increased. Moreover, Figures 4.1.6a, 4.1.6c, 4.1.7a and 4.1.7c demonstrate that for $\theta = 30^o, 54^o, 72^o$ the normalized mode I driving force parameters viz., SIF and SERR initially increase and then decrease in strip (I) while the opposite trend is observed in strip (II). However from

the Figures 4.1.6b, 4.1.6d, 4.1.7b and 4.1.7d, it can be observed that in the strips (I) and (II), the normalized mode II SIFs and SERRs show opposite nature to mode I case in respective strips.

Hence, if the crack orientation angle changes from acute to obtuse and the crack crosses the interface of the considered bonded structure, the mode I and mode II SIFs and SERRs are changed significantly.

4.1.6.4 Effect of strip thickness ratio

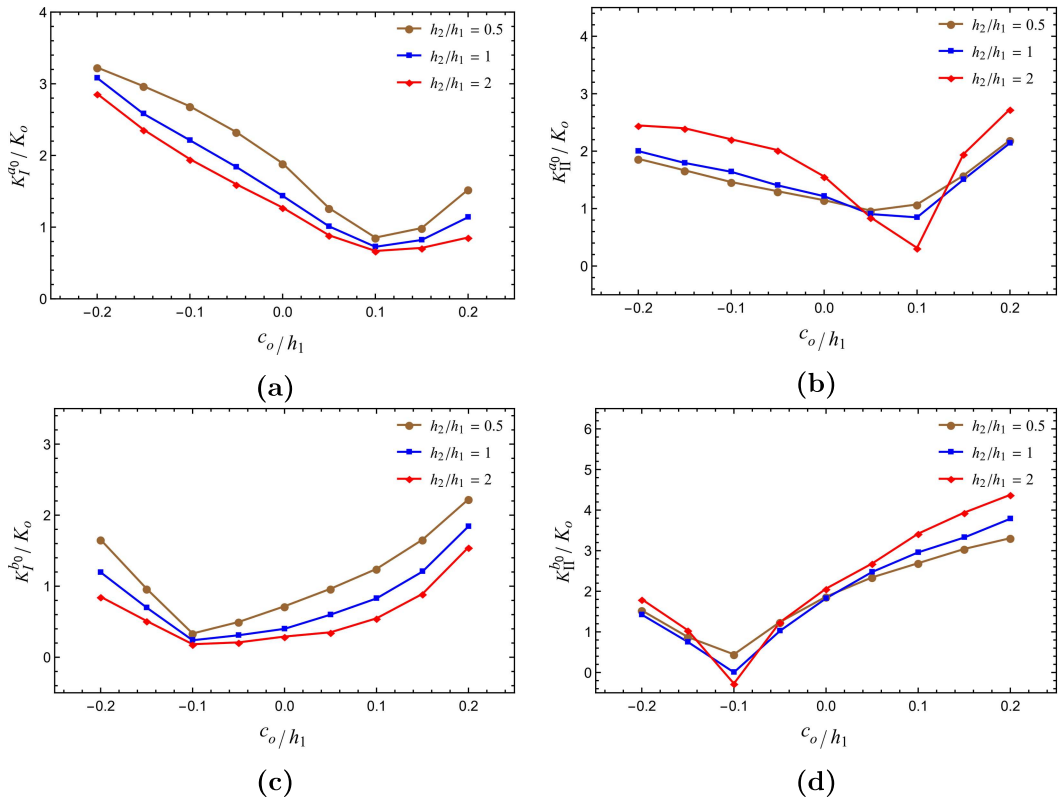

Figure 4.1.8: Plots showing normalized mode I and mode II crack tip SIFs as a function of normalized crack centre c_0/h_1 for different values of strips' thickness ratio h_2/h_1.

Here, the consequence of the thickness of strips on SIFs and SERRs is disserted. For $h_2/h_1 = 0.5, 1, 2$, the influence of thickness is studied as the crack

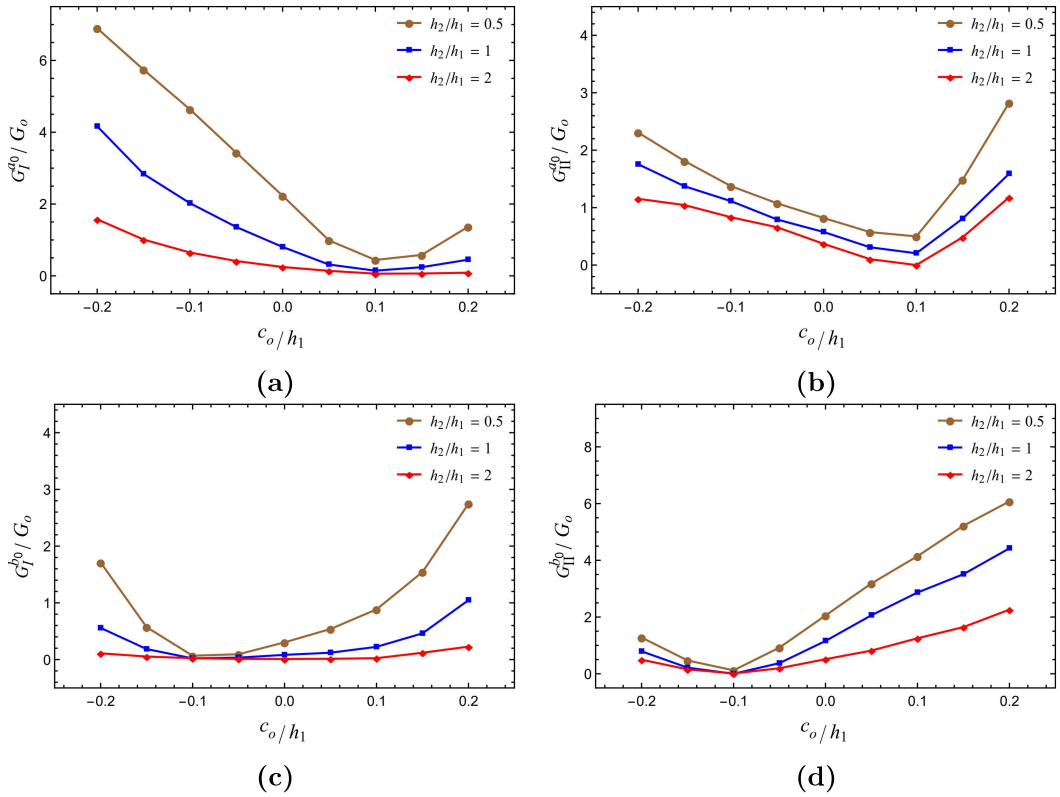

Figure 4.1.9: Plots showing normalized mode I and mode II crack tip SERRs as a function of normalized crack centre c_0/h_1 for different values of strips' thickness ratio h_2/h_1.

crosses the interface under thermo-mechanical loading. Figures 4.1.8 and 4.1.9 show that contrary to the previous cases, when the crack tips a_0 and b_0 cross the interface for $c_0/h_1 = 0.1$ and -0.1, respectively the behavior of normalized crack tip SIFs and SERRs for different values of strips' thickness ratio remain same in both the strips i.e., as h_2/h_1 decreases the driving force parameters at the crack tips increase in both the strips except for mode II crack tip SIFs. It can be seen from Figures 4.1.8b and 4.1.8d that for distinct values of strips' thickness ratio, the mode II SIF at the crack tips changes significantly. This shows that it is important to study the behavior of SIFs along with SERRs.

In general it can be said that for the thin lower strip the magnitudes of

driving force parameters are greater than those for the thick upper strip except for mode II crack tip SIFs.

4.1.6.5 Effect of stiffness parameter ratio

Figure 4.1.10 demonstrates that with varying stiffness parameter, the mode I and mode II SIFs show complex behavior. However for $c_0/h_1 = 0.1$ and -0.1 when crack tips a_0 and b_0 reach the interface the SIFs in most of the cases attain their extremum values.

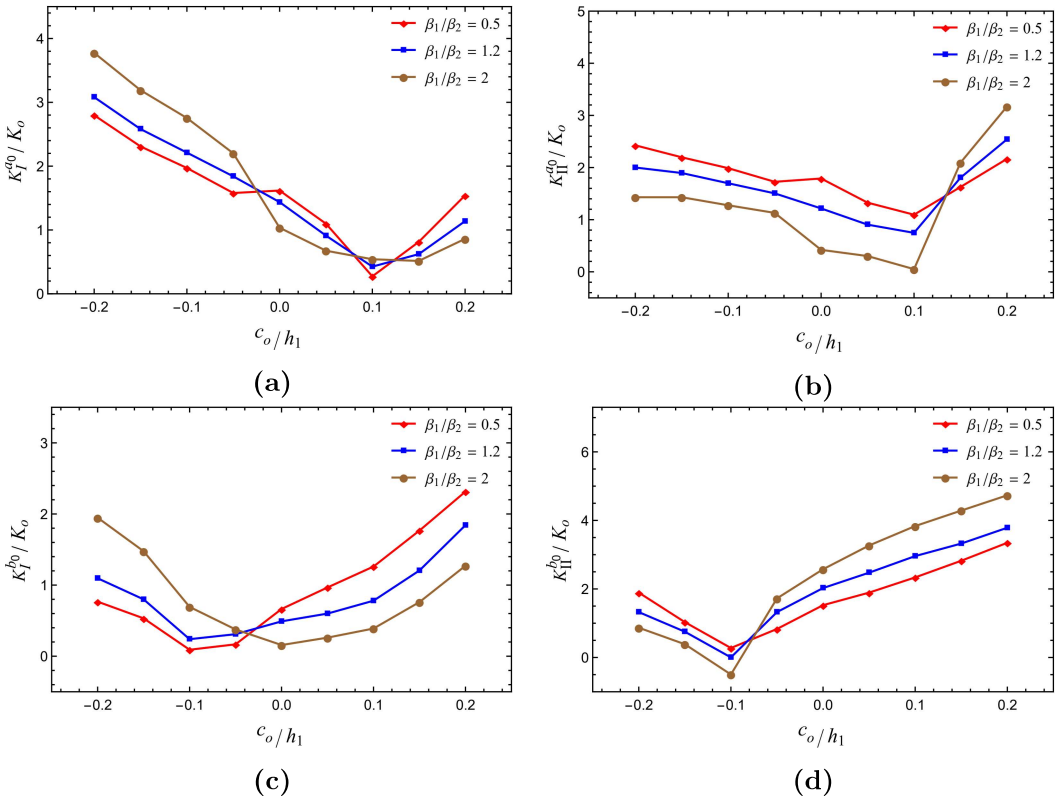

Figure 4.1.10: Plots showing normalized mode I and mode II crack tip SIFs as a function of normalized crack centre c_0/h_1 for different values of stiffness parameter ratio β_1/β_2.

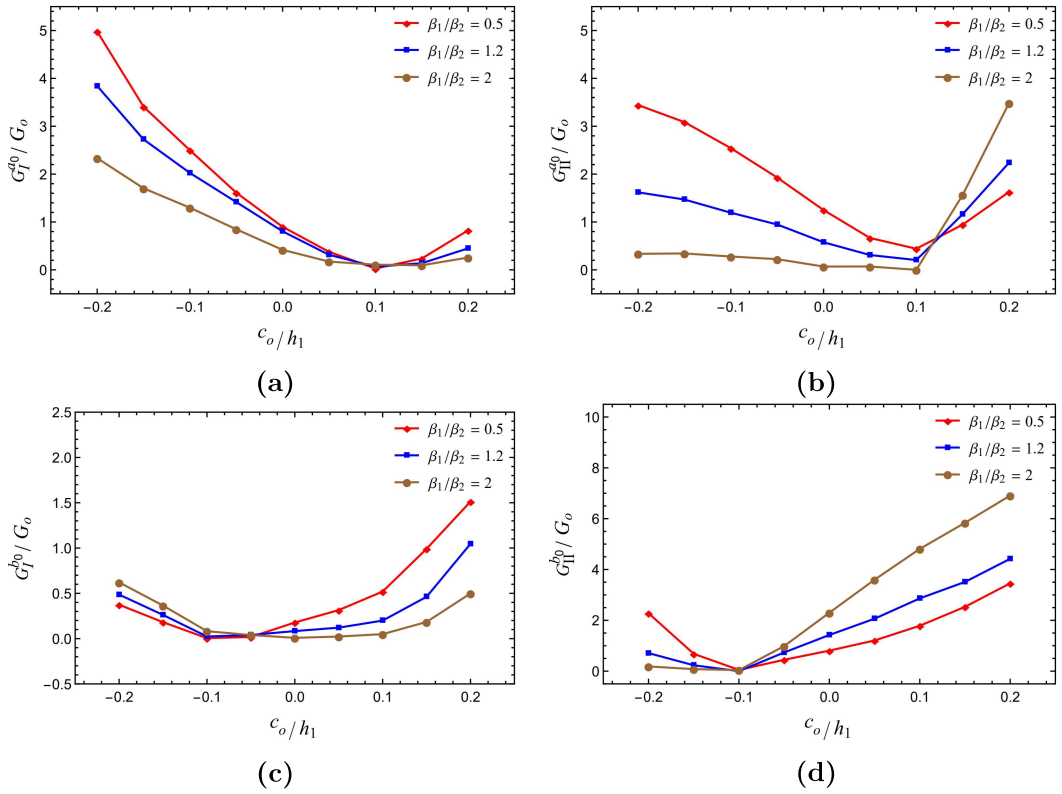

Figure 4.1.11: Plots showing normalized mode I and mode II crack tip SERRs as a function of normalized crack centre c_0/h_1 for different values of stiffness parameter ratio β_1/β_2.

The behaviors of normalized mode I and mode II SERRs for the distinct values of stiffness parameter ratio are presented in Figure 4.1.11. When the crack crosses the interface from the upper strip to the lower strip and propagates further the values of normalized SERRs at the crack tips attain their minimum at the interface. Figure 4.1.11a illustrates that for increasing values of β_1/β_2 viz. $0.5, 1.2, 2$, the normalized mode I SERR at the crack tip a_0 decreases in both the strips whereas Figure 4.1.11c shows that SERR at the crack tip b_0 increases with increasing values of β_1/β_2 in strip (I) while the opposite behavior is observed for the strip (II). Further, from the Figures 4.1.11b and 4.1.11d, it is observed that for strip (I) mode II SERRs at the crack tips increase for compliant upper strip and stiffened lower strip.

The above-mentioned discussion shows that the consideration of the stiffness parameter is important factor to study the behavior of mode I and mode II crack tip SIFs and SERRs for an arbitrary-oriented crack that crosses the interface under thermo-mechanical loading.

4.1.6.6 Effect of heat conduction parameter ratio

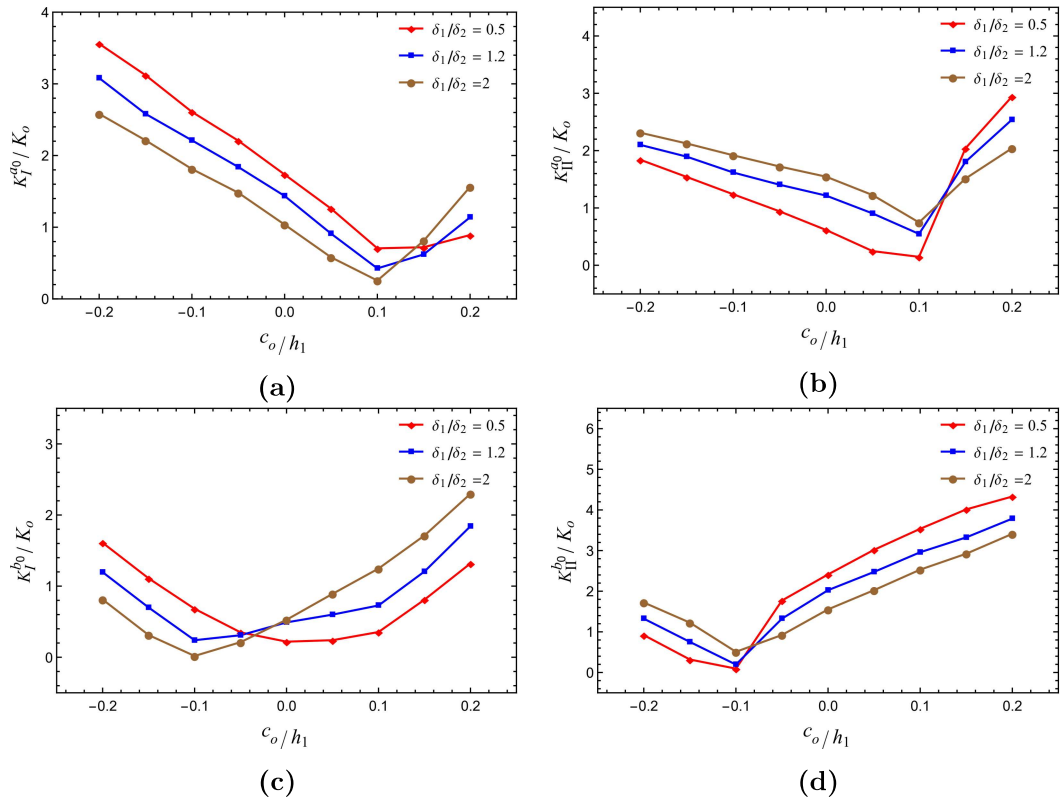

Figure 4.1.12: Influence of heat conduction parameter ratio δ_1/δ_2 on normalized mode I and mode II crack tip SIFs.

Figures 4.1.12 and 4.1.13 show the effect of heat conduction parameter ratio δ_1/δ_2 on mode I and mode II SERRs for the considered model. It can be noted from the Figures 4.1.12a, 4.1.12c, 4.1.13a and 4.1.13c that for increasing values of δ_1/δ_2, the magnitudes of mode I crack tip SIFs and SERRs decrease in strip (I) while

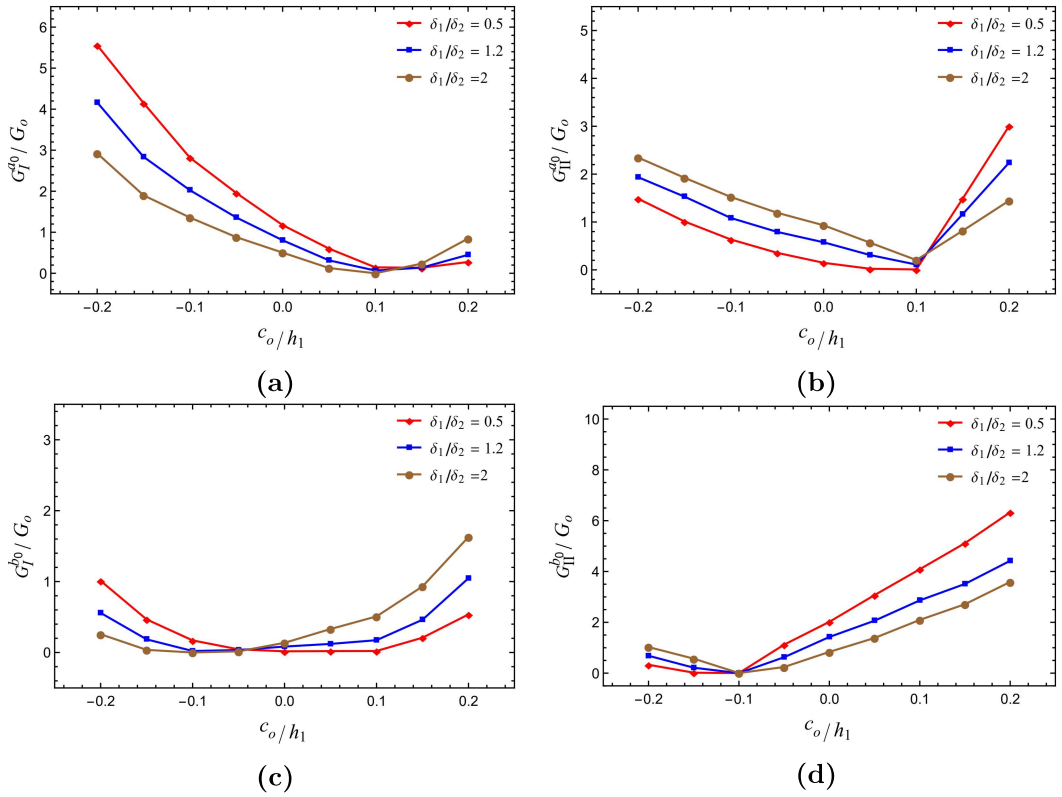

Figure 4.1.13: Influence of heat conduction parameter ratio δ_1/δ_2 on normalized mode I and mode II crack tip SERRs.

those increase in case of strip (II) with the said ratio. The opposite nature is found for mode II crack tip SIFs and SERRs.

Therefore the importance of the heat conduction parameter on driving force parameters can not be ignored.

4.1.6.7 Effect of thermal expansion coefficient ratio

The effect of the thermal expansion coefficient ratio γ_1/γ_2 on the driving force parameters is contrary to the heat conduction parameter ratio δ_1/δ_2 for both the strips and for both mode I and II as observed from Figures 4.1.14 and 4.1.15.

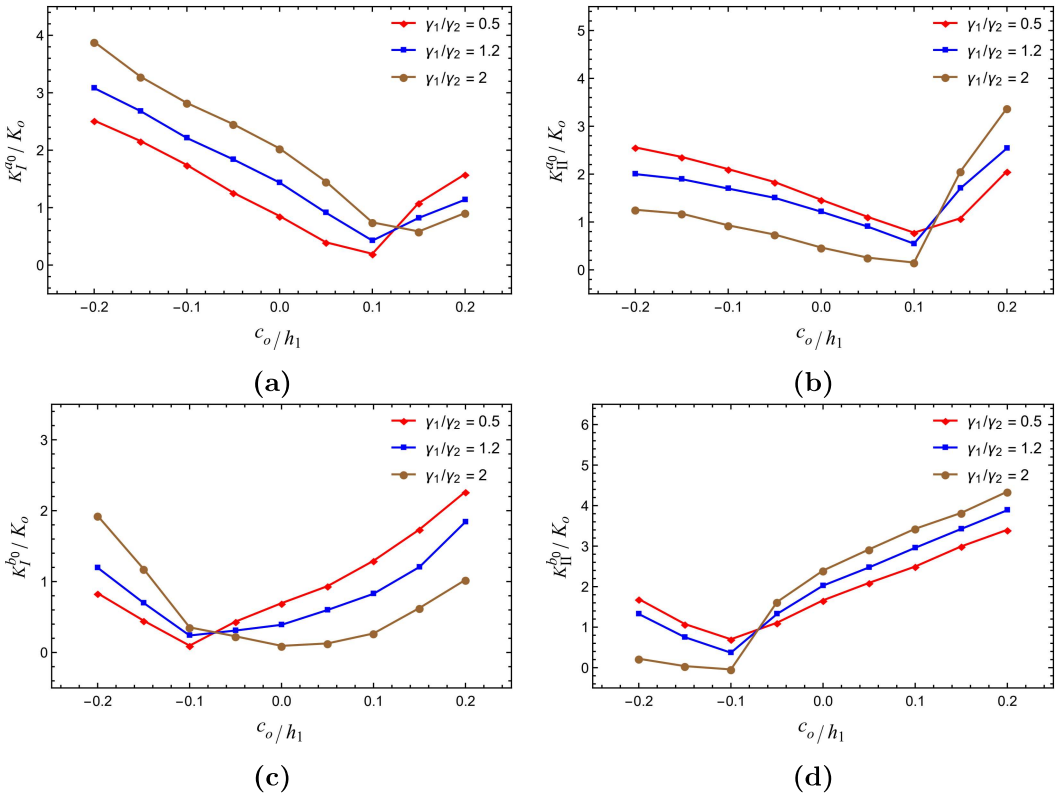

Figure 4.1.14: Influence of thermal expansion coefficient ratio γ_1/γ_2 on normalized mode I and mode II crack tip SIFs.

4.1.7 Concluding remarks

The effects of various factors on the normalized mode I and mode II crack tip SIFs and SERRs for an arbitrary-oriented crack that passes through the interface of bonded finitely thick functionally graded strips under thermo-mechanical loading have been discussed in this chapter. During the numerical calculation, a numerical strategy known as the Schmidt method is chosen. The findings of this investigation are also validated for a specific case. Followings are the findings of the present study:

1. The expressions of mode I and mode II crack tip SIFs and SERRs are obtained.

2. The pictorial representations of normalized mode I and mode II crack tip SIFs and SERRs indicate that, under the effects of various parameters, their

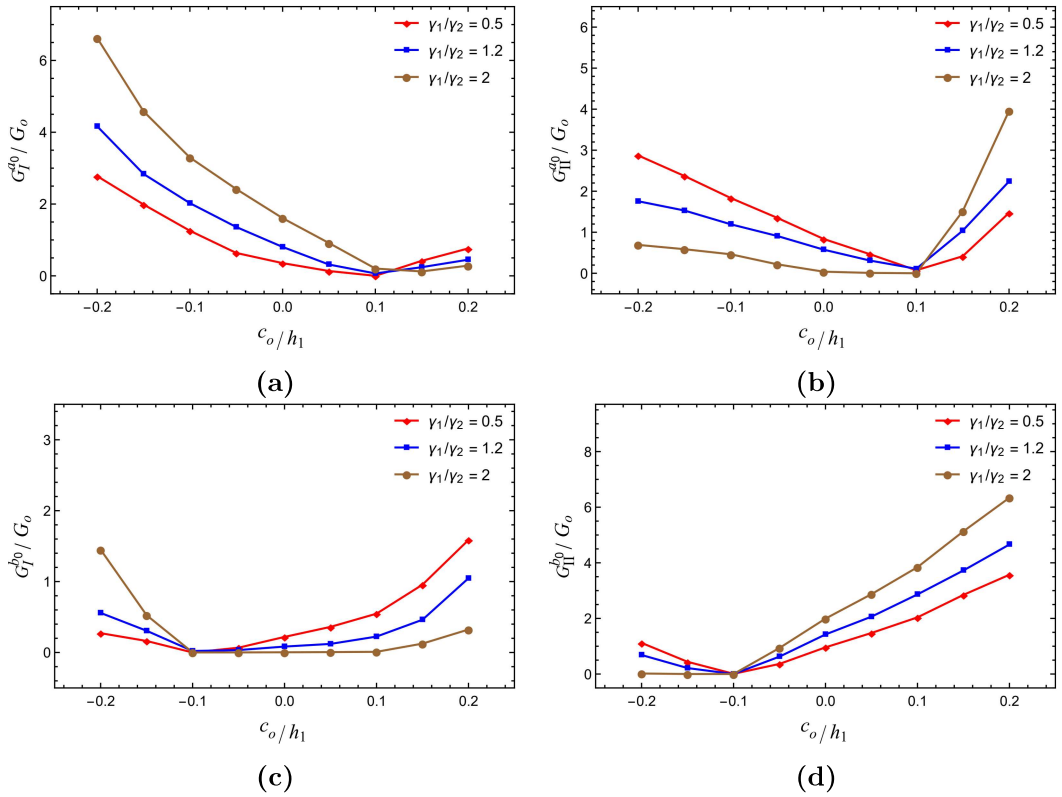

Figure 4.1.15: Influence of thermal expansion coefficient ratio γ_1/γ_2 on normalized mode I and mode II crack tip SERRs.

magnitudes initially decrease as the crack crosses the interface and then begin to increase after crossing the interface, i.e., driving force parameters reach their minimum at the interface.

3. As the angled crack crosses the interface, its insulating nature has a considerable impact on the driving force parameters viz., SIF and SERR. For monotonic values of the crack insulating parameter, the crack tip SIFs and SERRs for mode I behave differently from those of mode II.

4. The driving force parameters for both modes reach their extremum values with the opposite trend inside the strips (I) and (II) as the crack orientation angle shifts from acute to obtuse.

5. The graphical displays of SIFs and SERRs at the crack tips under the impact of strips' thickness show that they have different characteristics from one another. The behavior of crack tip SIFs is found to be complex for varying strips' thicknesses. As a result, it is crucial to investigate the nature of the driving force parameter SIF for the model under consideration.

6. The compliant and stiffened properties of upper and lower strips affect the behavior of SIFs and SERRs.

7. The behavior of the driving force parameters is contrary in nature for both the strips and for both the modes, as shown in graphical presentations of the mode I and mode II crack tip SIFs and SERRs under the influence of heat conduction and thermal expansion coefficient ratios. Therefore, it is crucial to consider how these characteristics affect SIFs and SERRs.

****

4.2 Schmidt method to study the disturbance of steady-state heat flows by an arbitrary-oriented crack in bonded functionally graded strips

4.2.1 Introduction

To achieve the performance and reliability standards of contemporary engineering domains, structural components constructed of non-homogeneous materials are required. Due to the composition, which combines a ceramic micro-crystalline coating with a metallic substrate, composite materials like thermal barrier coating are now employed to meet the demands of mechanical strength and thermal insulability. Additionally, high heat, corrosion resistance, and mechanical toughness are needed for gas turbine engine blades. Machine tools need high levels of toughness and wear resistance in their gears and bearings. Composites created from different materials are employed to fulfill these needs. The non-homogeneous materials created in this manner have desired characteristics in their constituent parts. These characteristics can also include a high degree of mechanical strength, toughness, thermal oxidation resistance, and corrosion resistance. To increase the resilience of composite constructions, the idea of functionally graded materials (FGMs) is utilized. The thermal expansion coefficient can be changed in the preferred direction by utilizing FGM features such as elastic modulus and Poisson's ratio.

It is crucial to take structural reliability into account while creating FGM structures, especially for high temperatures applications. Few studies [84, 103, 112, 119] have taken care of fracture difficulties in composites built of FGM materials under the thermal influence. In [102], the interaction between three collinear Griffith cracks in an infinite functionally graded media exposed to thermomechanical loading

was examined. A fully insulated crack in a FGM strip was taken into consideration, and the impact of the material's non-homogeneity on temperature distribution and stress intensity factors (SIFs) is explored in [88]. The SIFs for embedded and surface cracks for a FGM strip under thermal or residual loads are discussed in [37]. The steady-state heat conduction problem was investigated by [10, 11] for an interfacial crack in different anisotropic materials. In [17], the steady-state heat flow problem for a crack perpendicular to the graded interfacial zone in bonded media was discussed. In [18], the extension of this issue for a crack with an arbitrary orientation under both vertical and horizontal heat flows was taken into consideration. It was discussed in [16] how a heat conduction problem in an infinite FGM plane could be impacted by a crack that could be randomly orientated and partially insulated. The identical issue with a perfectly insulated crack was researched in [110]. In [103], the anti-plane loading-induced transient behavior of three collinear cracks in a composite structure made of FGM was investigated.

FGM layered structures, such as functionally graded coated substrate systems, are now commonly employed in engineering applications because of their effectiveness in avoiding heat penetration, wear, and corrosion. Due to the gradual differences in their properties, FGM layered structures have the potential to improve reliability and durability as compared to traditional discrete layered or coating systems [46, 47, 49]. Studying the fracture behavior of FGMs' layered structure is crucial since fracture is a significant mode of failure. In addition to the fracture issues caused by vertical, embedding, and interfacial cracks, it is also feasible for the crack's tip to cross the FGM layered structure's interface and spread into the following layers [15, 63, 69].

To handle crack problems in FGMs, numerous researchers have used a variety of numerical approaches, including the dislocation density function method,

extended finite element method, and phase-field finite element method [70, 83, 102, 103, 108, 109]. Apart from these techniques, the Schmidt method is employed in this investigation. The Schmidt method does not demand the same treatment of singular integral equations' unknown variables as dislocation density functions as used in the aforementioned investigations. The benefit of the Schmidt approach is that it works successfully by taking into account the first few terms of the infinite series of Jacobi polynomials [77, 121]. The technique has a restriction if one takes into account the series' terms in large numbers as the resulting matrix is difficult to handle.

In this study, an effort has been made to investigate the fracture issue of crack that crosses the interface of the functionally graded layered structure. Consideration is given to a randomly oriented partially insulated crack. According to Figure 4.2.1, the crack center is located at the interface of the joint of functionally graded strips under the horizontal and vertical components of heat flow. A boundary value problem is transformed into singular integral equations by using the superposition method and integral transformation. The jump of temperature and displacements over crack surfaces are expressed as a series of Jacobi polynomials in the present study to derive the analytical expressions of crack tip HFIFs and mode I and mode II TSIFs employing the Schmidt method. The thermal effect's singularity indicates that during the process of heat conduction, energy is concentrated around the crack. Such energy intensification may have an adverse impact on heat dissipation. To signify the local energy accumulation it is important to study crack tip HFIFs and TSIFs. The chapter's unique feature is a graphical analysis of the heat flow disturbance brought on by an angled partially insulated crack that crosses the interface of bonded FGM strips through HFIFs and TSIFs. Therefore, in contrast to earlier studies [46, 47, 102, 103], in which the cracks are either parallel or vertical to the

surface, this study takes into account an arbitrarily oriented crack. Additionally, the angled crack is located at the interface of bonded FGM strips rather than an infinite functionally graded medium [16, 110]. To verify the effectiveness and efficiency of the method employed in this study, the obtained results are compared with existing results [110] for a specific case. The HFIFs and TSIFs vs. crack orientation angle, crack insulation parameter, strips' width, and non-homogeneity parameters' ratio have been graphically depicted in the present study to show the impact of partially insulated arbitrary orientated crack on both components of heat flow.

4.2.2 Mathematical formulation of the problem

4.2.2.1 Schematic description

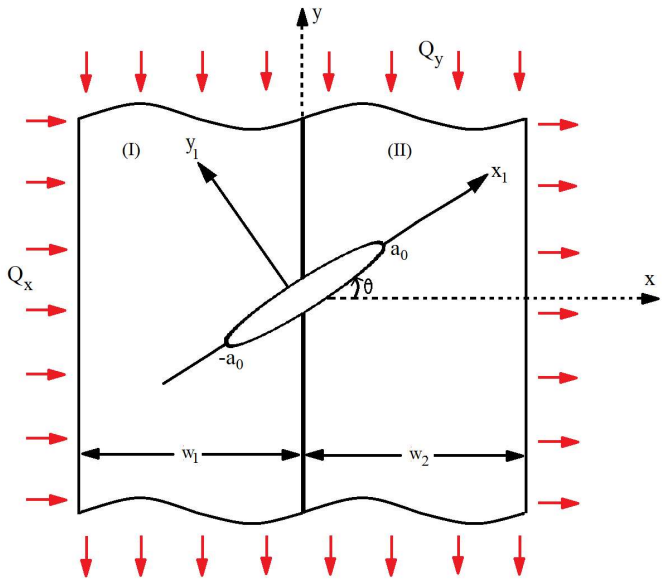

Figure 4.2.1: Schematic diagram of the problem.

Consider a composite structure that consists of two FGM strips of widths w_1 and w_2 respectively. As shown in Figure 4.2.1, a crack of arbitrary orientation and length $2a_0$ is aligned along the x_1-axis of the local coordinate system $x_1o_1y_1$, with

the center of the crack located at the origin of the global coordinate system xoy. The crack axis forms an angle θ with the $x-$axis of the global coordinate system. Steady-state heat fluxes Q_x and Q_y are applied to the composite structure in the horizontal and vertical directions, respectively. The notations (I) and (II) designate the left and right FGM strips, which occupy the regions $\{-w_1 \leq x \leq 0, -\infty \leq y \leq \infty\}$ and $\{0 \leq x \leq w_2, -\infty \leq y \leq \infty\}$, respectively.

Since the Poisson's ratio has a small range of variation [37, 103], in this study it will remain constant. The thermal thermal conductivity coefficients k_n, shear moduli μ_n and thermal expansion coefficients α_n are calculated in the xoy coordinate system by

$$k_n(x) = k_{0n}\,\exp(\delta_n x),\ \mu_n(x) = \mu_{0n}\,\exp(\beta_n x),\ \alpha_n(x) = \alpha_{0n}\,\exp(\gamma_n x), \tag{4.2.1}$$

and in the $x_1o_1y_1$ coordinate system those are expressed as

$$k_n(x_1, y_1) = k_{0n}\,\exp(\delta_{n1}x_1 + \delta_{n2}y_1), \tag{4.2.2}$$

$$\mu_n(x_1, y_1) = \mu_{0n}\,\exp(\beta_{n1}x_1 + \beta_{n2}y_1), \tag{4.2.3}$$

$$\alpha_n(x_1, y_1) = \alpha_{0n}\,\exp(\gamma_{n1}x_1 + \gamma_{n2}y_1), \tag{4.2.4}$$

where δ_n, β_n and γ_n are the heat conductivity, stiffness and thermal conductivity parameters, $\delta_{n1} = \delta_n \cos(\theta)$, $\delta_{n2} = -\delta_n \sin(\theta)$, $\beta_{n1} = \beta_n \cos(\theta)$, $\beta_{n2} = -\beta_n \sin(\theta)$, $\gamma_{n1} = \gamma_n \cos(\theta)$ and $\gamma_{n2} = -\gamma_n \sin(\theta)$. Note that in this study $n = 1, 2$ correspond to strips (I) and (II), respectively. It is further assumed that both thermal and material properties are continuous at the interface.

4.2.2.2 Governing equations and boundary conditions

Employing the superposition approach, the following equations determine the temperature θ, heat flux q, displacement (u, v) and stress component σ in the xoy coordinate system

$$\theta_n(x,y) = \theta_n^{(1)}(x,y) + \theta_n^{(2)}(x_1,y_1), \tag{4.2.5}$$

$$\begin{bmatrix} q_{nx}(x,y) \\ q_{ny}(x,y) \end{bmatrix} = \begin{bmatrix} q_{nx}^{(1)}(x,y) \\ q_{ny}^{(1)}(x,y) \end{bmatrix} + \begin{bmatrix} \cos(\theta) & -\sin(\theta) \\ \sin(\theta) & \cos(\theta) \end{bmatrix} \begin{bmatrix} q_{nx_1}^{(2)}(x_1,y_1) \\ q_{ny_1}^{(2)}(x_1,y_1) \end{bmatrix}, \tag{4.2.6}$$

$$\begin{bmatrix} u_n(x,y) \\ v_n(x,y) \end{bmatrix} = \begin{bmatrix} u_n^{(1)}(x,y) \\ v_n^{(1)}(x,y) \end{bmatrix} + \begin{bmatrix} \cos(\theta) & -\sin(\theta) \\ \sin(\theta) & \cos(\theta) \end{bmatrix} \begin{bmatrix} u_n^{(2)}(x_1,y_1) \\ v_n^{(2)}(x_1,y_1) \end{bmatrix}, \tag{4.2.7}$$

$$\begin{bmatrix} \sigma_{nxx}(x,y) \\ \sigma_{nxy}(x,y) \\ \sigma_{nyy}(x,y) \end{bmatrix} = \begin{bmatrix} \sigma_{nxx}^{(1)}(x,y) \\ \sigma_{nxy}^{(1)}(x,y) \\ \sigma_{nyy}^{(1)}(x,y) \end{bmatrix} + \begin{bmatrix} \cos^2(\theta) & \sin^2(\theta) & -\sin(2\theta) \\ \sin(2\theta)/2 & -\sin(2\theta)/2 & \cos(2\theta) \\ \sin^2(\theta) & \cos^2(\theta) & \sin(2\theta) \end{bmatrix} \begin{bmatrix} \sigma_{nx_1x_1}^{(2)}(x_1,y_1) \\ \sigma_{ny_1y_1}^{(2)}(x_1,y_1) \\ \sigma_{nx_1y_1}^{(2)}(x_1,y_1) \end{bmatrix}, \tag{4.2.8}$$

where $n = 1, 2$ and in this study superscript (1) denotes the bonded structure without the crack which is named as State A and superscript (2) denotes the bonded structure with a crack denoted by State B. The expressions of heat flux and stresses in terms of temperature and displacements are given in [18, 103]. Equations (4.2.5)-(4.2.8) can be expressed in the $x_1o_1y_1$ coordinate system by using the relationship between global and local coordinate systems as

$$\begin{bmatrix} x \\ y \end{bmatrix} = \begin{bmatrix} \cos(\theta) & -\sin(\theta) \\ \sin(\theta) & \cos(\theta) \end{bmatrix} \begin{bmatrix} x_1 \\ y_1 \end{bmatrix}. \tag{4.2.9}$$

The steady state heat conduction equations along with the boundary conditions are given by

State A: $$\frac{\partial}{\partial x}q^{(1)}_{nx}(x,y)+\frac{\partial}{\partial y}q^{(1)}_{ny}(x,y)=0. \tag{4.2.10}$$

State B: $$\frac{\partial}{\partial x_1}q^{(2)}_{nx_1}(x_1,y_1)+\frac{\partial}{\partial y_1}q^{(2)}_{ny_1}(x_1,y_1)=0. \tag{4.2.11}$$

$$\theta_1(0,y)=\theta_2(0,y), \qquad q_{1x}(0,y)=q_{2x}(0,y), \qquad |y|<\infty \tag{4.2.12}$$

$$q_{1x}(-w_1,y)=Q_x, \qquad q_{2x}(w_2,y)=Q_x, \qquad |y|<\infty \tag{4.2.13}$$

$$q_{ny_1}(x_1,0)=-k_n(x_1,0)[\sin(\theta)Q_x+\cos(\theta)Q_y]-h_c[\theta_n(x_1,0^+)-\theta_n(x_1,0^-)], \ |x_1|<a_0, \tag{4.2.14}$$

Equation (4.2.12) represents the continuity conditions of the temperature and heat flux about the interface $x=0$. Equation (4.2.13) indicates the heat flux applied at the boundaries $x=-w_1$ and $x=w_2$. The heat flux on the crack surface in the local coordinate system is given by equation (4.2.14) where h_c is the crack surface heat conductance [18]. Note that $h_c=0$ indicates completely insulated crack and $h_c>0$ indicates partially insulated crack.

The thermo-elasticity equations together with the boundary conditions are given by

State A: $$\frac{\partial}{\partial x}\sigma^{(1)}_{nxx}(x,y)+\frac{\partial}{\partial y}\sigma^{(1)}_{nxy}(x,y)=0, \tag{4.2.15}$$

$$\frac{\partial}{\partial x}\sigma^{(1)}_{nxy}(x,y)+\frac{\partial}{\partial y}\sigma^{(1)}_{nyy}(x,y)=0. \tag{4.2.16}$$

State B: $$\frac{\partial}{\partial x_1}\sigma^{(2)}_{nx_1x_1}(x_1,y_1)+\frac{\partial}{\partial y_1}\sigma^{(2)}_{nx_1y_1}(x_1,y_1)=0, \tag{4.2.17}$$

$$\frac{\partial}{\partial x_1}\sigma^{(2)}_{nx_1y_1}(x_1,y_1)+\frac{\partial}{\partial y_1}\sigma^{(2)}_{ny_1y_1}(x_1,y_1)=0. \tag{4.2.18}$$

$$\sigma_{1xx}(0,y)=\sigma_{2xx}(0,y), \qquad \sigma_{1xy}(0,y)=\sigma_{2xy}(0,y), \qquad |y|<\infty \tag{4.2.19}$$

$$u_1(0,y)=u_2(0,y), \qquad v_1(0,y)=v_2(0,y), \qquad |y|<\infty \tag{4.2.20}$$

$$\sigma_{1xx}(-w_1,y)=0, \qquad \sigma_{1xy}(-w_1,y)=0, \qquad |y|<\infty \tag{4.2.21}$$

$$\sigma_{2xx}(w_2,y)=0, \qquad \sigma_{2xy}(w_2,y)=0, \qquad |y|<\infty \tag{4.2.22}$$

$$\sigma_{ny_1y_1}(x_1,0)=0, \qquad \sigma_{nx_1y_1}(x_1,0)=0, \qquad |x_1|< a_0. \tag{4.2.23}$$

Equations (4.2.19) and (4.2.20) represent the continuity of the displacements and stresses at the interface $x=0$. Equations (4.2.21) and (4.2.22) denote the traction free conditions at the boundaries $x=-w_1$ and $x=w_2$. Equation (4.2.23) represents that no tractions are applied at the crack surface.

4.2.3 Solution of temperature field

4.2.3.1 Temperature field of the State A

Employing Fourier transform to y in equation (4.2.10), the temperature field for State A can be written as

$$\theta_n^{(1)}(x,y)=\frac{1}{2\pi}\int_{-\infty}^{\infty}\sum_{j=1}^{2}A_{nj}^{(1)}(\alpha)\,\exp(\lambda_{nj}^{(1)}(\alpha)x-i\alpha y)d\alpha, \tag{4.2.24}$$

where α stands for the variable related to Fourier transform, $A_{nj}^{(1)}(\alpha)$ are unknown functions of α and $\lambda_{nj}^{(1)}(\alpha)$ are determined by

$$\lambda_{nj}^{(1)}(\alpha)=\left[-\delta_n+(-1)^j\sqrt{\delta_n^2+4\alpha^2}\right]/2, \qquad n=1,2; \quad j=1,2. \tag{4.2.25}$$

4.2.3.2 Temperature field of the State B

Employing Fourier transform to x_1 in equation (4.2.11), the temperature field above and below the cracks' region can be given by

$$\theta_n^{(2)}(x_1,y_1)=\begin{cases}\frac{1}{2\pi}\int_{-\infty}^{\infty}\sum_{j=1}^{2}A_{nj}^{(2)}(s)\,\exp(\lambda_{nj}^{(2)}(s)y_1-isx_1)ds, & y_1>0,\\ \frac{1}{2\pi}\int_{-\infty}^{\infty}\sum_{j=1}^{2}A_{nj+2}^{(2)}(s)\,\exp(\lambda_{nj}^{(2)}(s)y_1-isx_1)ds, & y_1<0,\end{cases}\tag{4.2.26}$$

where s is the Fourier transform variable, $A_{nj}^{(2)}(s)$ are unknown functions of s and $\lambda_{nj}^{(2)}(s)$ are determined by

$$\lambda_{nj}^{(2)}(s)=\left[-\delta_{n2}+(-1)^j\sqrt{\delta_{n2}^2+4(s^2+is\delta_{n1})}\right]/2.\tag{4.2.27}$$

Regularity [37, 103] and continuity conditions of the temperature field at $y_1=0$ give

$$A_{n4}^{(2)}(s)=\frac{\lambda_{n1}^{(2)}(s)}{\lambda_{n2}^{(2)}(s)}A_{n1}^{(2)}(s),\quad A_{nj}^{(2)}(s)=0,\quad j=2,3.\tag{4.2.28}$$

Expressing the jump of temperature across the crack surfaces by $\phi(x_1)$ as

$$\phi(x_1)=\theta_n^{(2)}(x_1,0^+)-\theta_n^{(2)}(x_1,0^-),\qquad n=1,2,\tag{4.2.29}$$

and by using the Inverse Fourier transform, $A_{nj}^{(2)}(s)$ $(j=1,4)$ can be given by

$$A_{n1}^{(2)}(s)=W_{n1}^{(2)}(s)\Phi(s),\qquad A_{n4}^{(2)}(s)=W_{n2}^{(2)}(s)\Phi(s),\qquad n=1,2,\tag{4.2.30}$$

where $\Phi(s)=\int_{-\infty}^{\infty}\phi(x_1)\,\exp(isx_1)dx_1$ and $W_{nk}^{(2)}(s)$ are given in Appendix D.

4.2.3.3 Numerical solution of integral equation related to temperature field

Utilizing the boundary conditions (4.2.12)-(4.2.13) the matrix form of the unknown functions is expressed as

$$\boldsymbol{X.A} = \boldsymbol{Q} + \int_{-\infty}^{\infty} \boldsymbol{S}\ \Phi(s)\ ds, \tag{4.2.31}$$

where $\boldsymbol{A} = \begin{bmatrix} A_{11}^{(1)}(\alpha) \\ A_{12}^{(1)}(\alpha) \\ A_{21}^{(1)}(\alpha) \\ A_{22}^{(1)}(\alpha) \end{bmatrix}$, $\boldsymbol{Q} = \begin{bmatrix} 0 \\ 0 \\ -Q_x\delta(\alpha)/k_1(-w_1) \\ -Q_x\delta(\alpha)/k_2(w_2) \end{bmatrix}$,

$$\boldsymbol{S} = \sum_{j=1}^{2} \begin{bmatrix} W_{2j}^{(2)}(s)I_{2j}(s,\alpha,0) - W_{1j}^{(2)}(s)I_{1j}(s,\alpha,0) \\ k_2(0)W_{2j}^{(2)}(s)FF_{2j}^{(2)}(s)I_{2j}(s,\alpha,0) - k_1(0)W_{1j}^{(2)}(s)FF_{1j}^{(2)}(s)I_{1j}(s,\alpha,0) \\ -W_{1j}^{(2)}(s)FF_{1j}^{(2)}(s)I_{1j}(s,\alpha,-w_1) \\ -W_{2j}^{(2)}(s)FF_{2j}^{(2)}(s)I_{2j}(s,\alpha,w_2) \end{bmatrix},$$

$$\boldsymbol{X} = \begin{bmatrix} 1 & 1 & -1 & -1 \\ k_1(0)\lambda_{11}^{(1)}(\alpha) & k_1(0)\lambda_{12}^{(1)}(\alpha) & -k_2(0)\lambda_{21}^{(1)}(\alpha) & -k_2(0)\lambda_{22}^{(1} \\ \lambda_{11}^{(1)}(\alpha)\ \exp(-\lambda_{11}^{(1)}(\alpha)w_1) & \lambda_{12}^{(1)}(\alpha)\ \exp(-\lambda_{12}^{(1)}(\alpha)w_1) & 0 & 0 \\ 0 & 0 & \lambda_{21}^{(1)}(\alpha)\ \exp(\lambda_{21}^{(1)}(\alpha)w_2) & \lambda_{22}^{(1)}(\alpha)\ \exp(\lambda_2^{(} \end{bmatrix}$$

$\boldsymbol{X}$ is a non singular matrix, $\delta(\alpha)$ indicates the dirac delta function and $I_{nj}(s,\alpha,x), FF_{nj}^{(2)}(s)$ are given by equations (D.0.2)-(D.0.4) of Appendix D. For simplicity rewrite $A_{nk}^{(1)}(\alpha)$ as

$$\begin{bmatrix} A_{11}^{(1)}(\alpha) \\ A_{12}^{(1)}(\alpha) \\ A_{21}^{(1)}(\alpha) \\ A_{22}^{(1)}(\alpha) \end{bmatrix} = \begin{bmatrix} A_1(\alpha) \\ A_2(\alpha) \\ A_3(\alpha) \\ A_4(\alpha) \end{bmatrix} + \int_{-\infty}^{\infty} \begin{bmatrix} AA_1(\alpha,s) \\ AA_2(\alpha,s) \\ AA_3(\alpha,s) \\ AA_4(\alpha,s) \end{bmatrix} \Phi(s)\ ds, \tag{4.2.32}$$

where $A_j(\alpha)$ and $AA_j(\alpha,s)$ are the elements corresponding to j^{th} row of the matrices $\boldsymbol{X^{-1}.Q}$ and $\boldsymbol{X^{-1}.S}$, respectively. The boundary condition (4.2.14) gives

$$\int_{-\infty}^{\infty} K_n(x_1,s)\ \Phi(s)\ ds = -2\pi\left[\sin(\theta)Q_x + \cos(\theta)Q_y\right] + R_n(x_1),\ |x_1|< a_0, \tag{4.2.33}$$

where $K_n(x_1,s),\ R_n(x_1)$ are given in Appendix D.

To solve the integral equation (4.2.33) a numerical method is taken into consideration because of the complex form of the kernel of the considered equation. The Schmidt method is used in this chapter to determine the unknown function $\phi(x_1)$ by expressing it as a series of Jacobi polynomials given by

$$\phi(x_1) = \begin{cases} \sum_{k=0}^{\infty} b_k P_k^{\left(\frac{1}{2},\frac{1}{2}\right)}\left(\frac{x_1}{a_0}\right)\left[1-\left(\frac{x_1}{a_0}\right)^2\right]^{\frac{1}{2}}, & |x_1|< a_0, \\ 0, & |x_1|> a_0, \end{cases} \tag{4.2.34}$$

where b_k is the unknown coefficient and $P_k^{\left(\frac{1}{2},\frac{1}{2}\right)}(x)$ stands for Jacobi polynomial. The application of Fourier transformation to the equation (4.2.34) gives

$$\Phi(s) = \sum_{k=0}^{\infty} \frac{b_k B_k G_k}{s} J_{k+1}\left(sa_0\right), \tag{4.2.35}$$

where $B_k = 2\sqrt{\pi}\frac{\Gamma\left(k+1+\frac{1}{2}\right)}{k!}$, $G_k = (-1)^k i^k$ and Γ, J_k stand for the Gamma and Bessel functions, respectively. Substituting equation (4.2.35) into equation (4.2.33) and integrating with respect to x_1 from $-a_0$ to x_1, equation (4.2.33) takes the form

$$\sum_{k=0}^{\infty} b_k\ E_{nk}(x_1) = S_n(x_1), \qquad |x_1|< a_0, \tag{4.2.36}$$

where $E_{nk}(x_1)$ and $S_n(x_1)$ are given in Appendix D. The solution of the equation (4.2.36) for the unknown coefficient b_k is determined by Schmidt method [77].

4.2.4 Solution of thermal stresses

4.2.4.1 Thermal stresses of the State A

The displacement components for the first state after solving equations (4.2.15) and (4.2.16) with the help of Fourier transform in y are given by

$$u_n^{(1)}(x,y) = \frac{1}{2\pi}\int_{-\infty}^{\infty}\sum_{j=1}^{4} B_{nj}^{(1)}(\alpha)C_{nj}^{(1)}(\alpha)\,\exp(\tau_{nj}^{(1)}(\alpha)x - i\alpha y)d\alpha + \frac{2\alpha_n(x)}{\pi}\int_{-\infty}^{\infty}\sum_{j=1}^{2} u_{tnj}^{(1)}(\alpha)\,\exp(\lambda_{nj}^{(1)}(\alpha)x - i\alpha y)d\alpha,$$

$$v_n^{(1)}(x,y) = \frac{1}{2\pi}\int_{-\infty}^{\infty}\sum_{j=1}^{4} B_{nj}^{(1)}(\alpha)\,\exp(\tau_{nj}^{(1)}(\alpha)x - i\alpha y)d\alpha + \frac{2\alpha_n(x)}{\pi}\int_{-\infty}^{\infty}\sum_{j=1}^{2} v_{tnj}^{(1)}(\alpha)\,\exp(\lambda_{nj}^{(1)}(\alpha)x - i\alpha y)d\alpha,$$

where α is the Fourier variable, $B_{nj}^{(1)}(\alpha)$ are unknown functions in α, $C_{nj}^{(1)}(\alpha)$, $u_{tnj}^{(1)}(\alpha)$, $v_{tnj}^{(1)}(\alpha)$ are given by equations (D.0.9)-(D.0.12) in Appendix D and $\tau_{nj}^{(1)}(\alpha)$ are determined by

$$\tau_{nj}^{(1)}(\alpha) = \frac{1}{2}\left(-\beta_n + (-1)^j\sqrt{4\alpha^2+\beta_n^2-4if_0\alpha\beta_n}\right),\ \tau_{n2}^{(1)}(\alpha) = \overline{\tau_{n1}^{(1)}(\alpha)},\ \tau_{n3}^{(1)}(\alpha) = \overline{\tau_{n4}^{(1)}(\alpha)},$$

where $n = 1,2;\ j = 1,4,\ f_0 = \sqrt{(3-k)/(1+k)}$ and $k = 3-4\nu, (3-4\nu)/(1+\nu)$ for plane strain and plane stress cases, respectively. The expressions of thermal stresses for State A are determined by using the relation between stresses and displacements.

4.2.4.2 Thermal stresses of the State B

Employing Fourier transform in equations (4.2.17) and (4.2.18) the expressions of displacement fields above and below the cracks' region are as follows

$$u_n^{(2)}(x_1,y_1)=\begin{cases}\frac{1}{2\pi}\int_{-\infty}^{\infty}\sum_{j=1}^{4}B_{nj}^{(2)}(s)C_{nj}^{(2)}(s)\,\exp(\tau_{nj}^{(2)}(s)y_1-isx_1)ds\\ +\frac{2\alpha_n(x_1,y_1)}{\pi}\int_{-\infty}^{\infty}u_{tn1}^{(2)}(s)\,\exp(\lambda_{n1}^{(2)}(s)y_1-isx_1)ds, & y_1>0,\\ \frac{1}{2\pi}\int_{-\infty}^{\infty}\sum_{j=1}^{4}B_{nj+4}^{(2)}(s)C_{nj}^{(2)}(s)\,\exp(\tau_{nj}^{(2)}(s)y_1-isx_1)ds\\ +\frac{2\alpha_n(x_1,y_1)}{\pi}\int_{-\infty}^{\infty}u_{tn2}^{(2)}(s)\,\exp(\lambda_{n2}^{(2)}(s)y_1-isx_1)ds, & y_1<0,\end{cases}$$

$$v_n^{(2)}(x_1,y_1)=\begin{cases}\frac{1}{2\pi}\int_{-\infty}^{\infty}\sum_{j=1}^{4}B_{nj}^{(2)}(s)\,\exp(\tau_{nj}^{(2)}(s)y_1-isx_1)ds\\ +\frac{2\alpha_n(x_1,y_1)}{\pi}\int_{-\infty}^{\infty}v_{tn1}^{(2)}(s)\,\exp(\lambda_{n1}^{(2)}(s)y_1-isx_1)ds, & y_1>0,\\ \frac{1}{2\pi}\int_{-\infty}^{\infty}\sum_{j=1}^{4}B_{nj+4}^{(2)}(s)\,\exp(\tau_{nj}^{(2)}(s)y_1-isx_1)ds\\ +\frac{2\alpha_n(x_1,y_1)}{\pi}\int_{-\infty}^{\infty}v_{tn2}^{(2)}(s)\,\exp(\lambda_{n2}^{(2)}(s)y_1-isx_1)ds, & y_1<0,\end{cases}$$

where s is the transformed variable, $B_{nj}^{(2)}(s)$ are unknown functions in s, $C_{nj}^{(2)}(s)$, $u_{tnj}^{(2)}(s)$, $v_{tnj}^{(2)}(s)$ are given by equations (D.0.13)-(D.0.16) in Appendix D and $\tau_{nj}^{(2)}(s)$ are determined by

$$\tau_{nj}^{(2)}(s)=\left[-\sqrt{(\beta_{n2}+(-1)^{j+1}f_0\beta_{n1})^2+4s\,(s+i\beta_{n1}+(-1)^j if_0\beta_{n2})}-\beta_{n2}+(-1)^j f_0\beta_{n1}\right]/2,\ j=1,2,$$
$$\tau_{nj}^{(2)}(s)=\left[\sqrt{(\beta_{n2}+(-1)^{j+1}f_0\beta_{n1})^2+4s\,(s+i\beta_{n1}+(-1)^j if_0\beta_{n2})}-\beta_{n2}+(-1)^j f_0\beta_{n1}\right]/2,\ j=3,4.$$

Analogous to the temperature field case, application of regularity conditions give $B_{nj}^{(2)}(s)=0$, $j=3,4,5,6$. Denoting the jump of the displacement components by

$$\psi_1(x_1)=u_n^{(2)}(x_1,0^+)-u_n^{(2)}(x_1,0^-),\quad \psi_2(x_1)=v_n^{(2)}(x_1,0^+)-v_n^{(2)}(x_1,0^-). \tag{4.2.37}$$

Utilizing Inverse Fourier transform in (4.2.37) and stress continuity condition at $y_1=0$, $B_{nj}^{(2)}(s)$ $(j=1,2,7,8)$ can be determined by the matrix given as follows

$$\boldsymbol{M.B} = \boldsymbol{T} + \boldsymbol{S_1} + \boldsymbol{S_2}, \tag{4.2.38}$$

where $\boldsymbol{M} = \begin{bmatrix} D^{(2)}_{n1}(s) & D^{(2)}_{n2}(s) & -D^{(2)}_{n3}(s) & -D^{(2)}_{n4}(s) \\ E^{(2)}_{n1}(s) & E^{(2)}_{n2}(s) & -E^{(2)}_{n3}(s) & -E^{(2)}_{n4}(s) \\ C^{(2)}_{n1}(s) & C^{(2)}_{n2}(s) & -C^{(2)}_{n3}(s) & -C^{(2)}_{n4}(s) \\ 1 & 1 & -1 & -1 \end{bmatrix}$, $\boldsymbol{B} = \begin{bmatrix} B^{(2)}_{n1}(s) \\ B^{(2)}_{n2}(s) \\ B^{(2)}_{n7}(s) \\ B^{(2)}_{n8}(s) \end{bmatrix}$,

$$\boldsymbol{T} = \begin{bmatrix} 4\alpha_n(x_1,0)(D^{'(2)}_{n4}(s) - D^{'(2)}_{n1}(s)) \\ 4\alpha_n(x_1,0)(E^{'(2)}_{n4}(s) - E^{'(2)}_{n1}(s)) \\ 4\alpha_n(x_1,0)(u^{(2)}_{tn4}(s) - u^{(2)}_{tn1}(s)) \\ 4\alpha_n(x_1,0)(v^{(2)}_{tn4}(s) - v^{(2)}_{tn1}(s)) \end{bmatrix}, \quad \boldsymbol{S_1} = \begin{bmatrix} 0 \\ 0 \\ \Psi_1(s) \\ 0 \end{bmatrix}, \boldsymbol{S_2} = \begin{bmatrix} 0 \\ 0 \\ 0 \\ \Psi_2(s) \end{bmatrix},$$

$$\Psi_1(s) = \int_{-\infty}^{\infty} \psi_1(x_1) e^{isx_1} dx_1 \quad \text{and} \quad \Psi_2(s) = \int_{-\infty}^{\infty} \psi_2(x_1) e^{isx_1} dx_1,$$

$\boldsymbol{M}$ is a non singular matrix, $D^{(2)}_{nj}(s)$, $E^{(2)}_{nj}(s)$, $D^{'(2)}_{nj}(s)$ and $E^{'(2)}_{nj}(s)$ are given in Appendix D. Rewritting the unknowns $B^{(2)}_{nj}(s)$ as

$$B^{(2)}_{nj}(s) = B^{(2)}_{1nj}(s) + B^{(2)}_{2nj}(s)\Psi_1(s) + B^{(2)}_{3nj}(s)\Psi_2(s), \tag{4.2.39}$$

where $B^{(2)}_{1nj}(s)$, $B^{(2)}_{2nj}(s)$ and $B^{(2)}_{3nj}(s)$ are the related to the matrices $\boldsymbol{M^{-1}.T}$, $\boldsymbol{M^{-1}.S_1}$ and $\boldsymbol{M^{-1}.S_2}$ respectively.

4.2.4.3 Numerical solution of integral equations related to stress field

The unknowns $B^{(1)}_{nj}(\alpha)$ can be expressed in terms of Φ, Ψ_1 and Ψ_2 with the aid of equations (4.2.19)-(4.2.22) and gives the following eight equations

$$\sum_{j=1}^{4} B_{nj}^{(1)}(\alpha) FE_{mnj}^{(1)}(\alpha)\, \exp(p_n w_n \tau_{nj}^{(1)}(\alpha)) = -\int_{-\infty}^{\infty} \left[\sum_{j=1}^{2} B_{nj}^{(2)}(s) + \sum_{j=3}^{4} B_{nj+4}^{(2)}(s)\right]$$
$$\times GH_{mnj}^{(2)}(s) S_{nj}(s, \alpha, p_n w_n) ds - 4\alpha_n(p_n w_n)\Bigg[\sum_{j=1}^{2} FE_{mnj}^{'(1)}(\alpha)\, \exp(p_n w_n \lambda_{nj}^{(1)}(\alpha))$$
$$-\int_{-\infty}^{\infty} (GH_{mn1}^{'(2)}(s) I_{n1}(s, \alpha, p_n w_n) + GH_{mn4}^{'(2)}(s) I_{n2}(s, \alpha, p_n w_n)) ds\Bigg], \tag{4.2.40}$$

$$\sum_{n=1}^{2}\sum_{j=1}^{4} p_{n+1}\mu_n(0) B_{nj}^{(1)}(\alpha) FE_{mnj}^{(1)}(\alpha) = \int_{-\infty}^{\infty} \sum_{n=1}^{2} p_n \mu_n(0) \left[\sum_{j=1}^{2} B_{nj}^{(2)}(s) + \sum_{j=3}^{4} B_{nj+4}^{(2)}(s)\right]$$
$$\times GH_{mnj}^{(2)}(s) S_{nj}(s, \alpha, 0) ds + 4\sum_{n=1}^{2} p_n \alpha_n(0)\mu_n(0)\Bigg[\sum_{j=1}^{2} FE_{mnj}^{'(1)}(\alpha)$$
$$-\int_{-\infty}^{\infty} (GH_{mn1}^{'(2)}(s) I_{n1}(s, \alpha, 0) + GH_{mn4}^{'(2)}(s) I_{n2}(s, \alpha, 0)) ds\Bigg], \tag{4.2.41}$$

$$\sum_{n=1}^{2}\sum_{j=1}^{4} p_{n+1} B_{nj}^{(1)}(\alpha) C1_{mnj}^{(1)}(\alpha) = \int_{-\infty}^{\infty} \sum_{n=1}^{2} p_n \left[\sum_{j=1}^{2} B_{nj}^{(2)}(s) + \sum_{j=3}^{4} B_{nj+4}^{(2)}(s)\right] JK_{mnj}^{(2)}(s)$$
$$\times S_{nj}(s, \alpha, 0) ds + 4p_n\alpha_n(0) \sum_{j=1}^{2} \left[uv_{tmnj}^{(1)}(\alpha) - \int_{-\infty}^{\infty} JK_{mnj}^{'(2)}(s) I_{nj}(s, \alpha, 0) ds\right], \tag{4.2.42}$$

where $m, n = 1, 2$, $p_n = (-1)^n$, $FE_{mnj}^{(1)}(\alpha)$, $FE_{mnj}^{'(1)}(\alpha)$, $GH_{mnj}^{(2)}(s)$, $GH_{mnj}^{'(2)}(s)$, $JK_{mnj}^{(2)}(s)$, $JK_{mnj}^{'(2)}(s)$, $C1_{mnj}^{(2)}(s)$, $uv_{tmnj}^{(1)}(\alpha)$ and $S_{nj}(s, \alpha, x)$ are given in Appendix D. Rewritting $B_{nj}^{(1)}(\alpha)$ as

$$B_{1j}^{(1)}(\alpha) = B_j(\alpha) + \int_{-\infty}^{\infty} (BB_j(\alpha, s)\Psi_1(s) + BBB_j(\alpha, s)\Psi_2(s)) ds, \tag{4.2.43}$$

$$B_{2j}^{(1)}(\alpha) = B_{j+4}(\alpha) + \int_{-\infty}^{\infty} (BB_{j+4}(\alpha, s)\Psi_1(s) + BBB_{j+4}(\alpha, s)\Psi_2(s)) ds, \tag{4.2.44}$$

where $j = 1, 2, 3, 4$, $B_j(\alpha)$, $BB_j(\alpha)$ and $BBB_j(\alpha)$ are the coefficients obtained by solving above equations. The following singular integral equations [46] are obtained after employing boundary condition (4.2.23)

$$\int_{-\infty}^{\infty}[N_{n11}(x_1,s)\ \Psi_1(s)+N_{n12}(x_1,s)\ \Psi_2(s)]\ ds=P_{1n}(x_1),\qquad |x_1|<a_0,\qquad (4.2.45)$$

$$\int_{-\infty}^{\infty}[N_{n21}(x_1,s)\ \Psi_1(s)+N_{n22}(x_1,s)\ \Psi_2(s)]\ ds=P_{2n}(x_1),\qquad |x_1|<a_0,\qquad (4.2.46)$$

where $N_{nmj}(x_1,s)$, $P_{mn}(x_1)$ are given in Appendix D. To obtain the solution of the integral equations (4.2.48) and (4.2.49), the unknown functions $\Psi_1(s)$ and $\Psi_2(s)$ are expressed as follows

$$\psi_n(x_1)=\begin{cases}\sum_{k=0}^{\infty}c_{nk}P_k^{\left(\frac{1}{2},\frac{1}{2}\right)}\left(\frac{x_1}{a_0}\right)\left[1-\left(\frac{x_1}{a_0}\right)^2\right]^{\frac{1}{2}}, & |x_1|<a_0,\\ 0, & |x_1|>a_0,\end{cases}\qquad (4.2.47)$$

where c_{nk} $(n=1,2)$ are the unknown coefficients to be determined. Similar to the temperature field case, these unknowns are determined by using the Schmidt method.

4.2.5 Driving force parameters

After getting the values of b_k and c_{nk}, the values of heat flux and stresses can be determined easily. Thus, the crack tip heat flux intensity factor (HFIF) is defined as [111]

$$K_H^{-a_0}=\lim_{x_1\to -a_0}\sqrt{2\pi(-x_1-a_0)}q_{1y_1}(x_1,0^+),\qquad (4.2.48)$$

$$K_H^{a_0}=\lim_{x_1\to a_0}\sqrt{2\pi(x_1-a_0)}q_{2y_1}(x_1,0^+).\qquad (4.2.49)$$

In terms of coefficients b_k, the expressions (4.2.48) and (4.2.49) can be found as

$$K_H^{-a_0} = -\frac{k_{01}}{2\pi\sqrt{a_0}}\,\exp(-\delta_{11}a_0)\sum_{k=0}^{\infty}\,b_k\;B_k, \tag{4.2.50}$$

$$K_H^{a_0} = -\frac{k_{02}}{2\pi\sqrt{a_0}}\,\exp(\delta_{21}a_0)\sum_{k=0}^{\infty}(-1)^k\;b_k\;B_k. \tag{4.2.51}$$

The mode I and mode II crack tip thermal stress intensity factors (TSIFs) are given by

$$K_I^{-a_0} = \lim_{x_1\to -a_0}\sqrt{2\pi(-x_1-a_0)}\sigma_{1y_1y_1}(x_1,0^+), \tag{4.2.52}$$

$$K_I^{a_0} = \lim_{x_1\to a_0}\sqrt{2\pi(x_1-a_0)}\sigma_{2y_1y_1}(x_1,0^+), \tag{4.2.53}$$

$$K_{II}^{-a_0} = \lim_{x_1\to -a_0}\sqrt{2\pi(-x_1-a_0)}\sigma_{1x_1y_1}(x_1,0^+), \tag{4.2.54}$$

$$K_{II}^{a_0} = \lim_{x_1\to a_0}\sqrt{2\pi(x_1-a_0)}\sigma_{2x_1y_1}(x_1,0^+), \tag{4.2.55}$$

which in terms of unknown coefficients c_{nk} are expressed as

$$K_I^{-a_0} = -\frac{2\mu_{01}\,\exp(-\mu_{11}a_0)}{(1+k)\pi\sqrt{a_0}}\sum_{k=0}^{\infty}\,c_{2k}\;B_k, \tag{4.2.56}$$

$$K_I^{a_0} = -\frac{2\mu_{02}\,\exp(\mu_{21}a_0)}{(1+k)\pi\sqrt{a_0}}\sum_{k=0}^{\infty}(-1)^k\,c_{2k}\;B_k, \tag{4.2.57}$$

$$K_{II}^{-a_0} = -\frac{2\mu_{01}\,\exp(-\mu_{11}a_0)}{(1+k)\pi\sqrt{a_0}}\sum_{k=0}^{\infty}\,c_{1k}\;B_k, \tag{4.2.58}$$

$$K_{II}^{a_0} = -\frac{2\mu_{02}\,\exp(\mu_{21}a_0)}{(1+k)\pi\sqrt{a_0}}\sum_{k=0}^{\infty}(-1)^k\,c_{1k}\;B_k. \tag{4.2.59}$$

4.2.6 Results and discussion

This section of the chapter deals with the graphical investigation of crack tip HFIFs and TSIFs vs. crack orientation angle, crack insulation parameter, the width of the

FGM strips, and non-homogeneity parameters for distinct values of crack angle.

During numerical computation $\lambda_b = h_c a_0/k_{01}$ is chosen for simplicity, where λ_b is called Biot number that describes the degree of crack surface partial insulation [7]. $K_{ox} = k_{01}Q_x\sqrt{a_0}$, $K_{oy} = k_{01}Q_y\sqrt{a_0}$, $K_{Ix} = K_{IIx} = 4\mu_{01}Q_x\sqrt{(a_0)^3}/(1+k)$ and $K_{Iy} = K_{IIy} = 4\mu_{01}Q_y\sqrt{(a_0)^3}/(1+k)$ are considered as normalizing parameters. In general $\lambda_b = 0.5$, $w_1/w_2 = 1$, $\delta_1/\delta_2 = 1$, $\beta_1/\beta_2 = 1$, $\gamma_1/\gamma_2 = 1$ and $\theta = \pi/4$ are taken for computation purpose. Even if one of those varies then the remaining parameters will have the mentioned fixed values. Moreover, for horizontal heat flow, $Q_x = Q_0, Q_y = 0$ and for vertical heat flow $Q_x = 0, Q_y = Q_0$ are considered.

4.2.6.1 Validation

To validate the present study obtained by using the Schmidt method, the results are compared with the results obtained in [110] in which the dislocation density function is introduced as an unknown variable. In [110] the heat transfer problem was studied

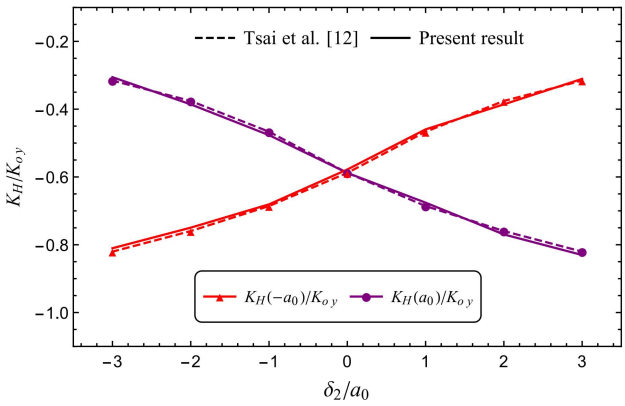

Figure 4.2.2: Comparison between the acquired and existing findings [110] of normalized crack tip HFIFs as a fuction of normalized heat conduction parameter δ_0/a_0 for a perfectly insulating angled crack in an infinite functionally graded medium.

for a perfectly insulated angled crack situated in an infinite FGM subject to uniform

heat flux. For $\theta = 54^o$, $w_1 = w_2 >> a_0$ and $\delta_1 = \delta_2 = \delta_0$, Figure 4.2.2 shows close proximity between the obtained results and the existing results.

4.2.6.2 Influence of crack orientation angle

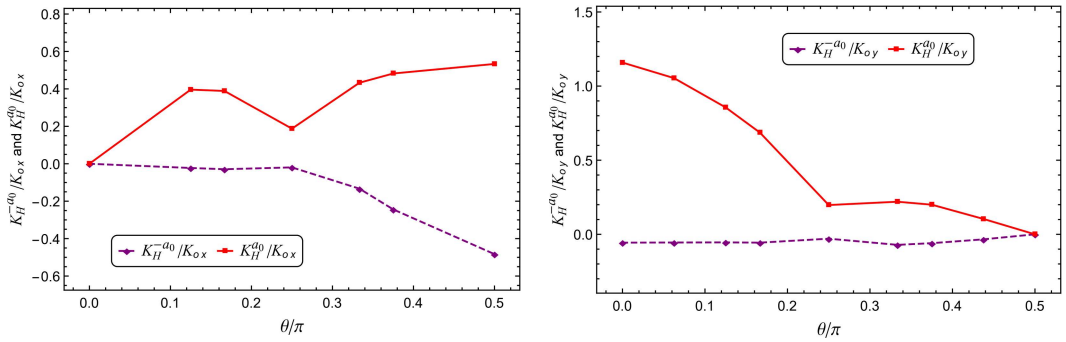

(a) **(b)**

Figure 4.2.3: Variations in normalized crack tip HFIFs subjected to (a) horizontal and (b) vertical heat flow for distinct values of normalized crack orientation angle θ/π.

In the Figures 4.2.3a and 4.2.3b, the effect of obliquity θ on the crack tip HFIFs are demonstrated for steady-state horizontal and vertical heat flows, respectively. From the Figure 4.2.3a it is clear that under horizontal heat flow, K_H at $-a_0$ increases as the crack angle increases from 0 to 0.25π and after $\theta = 0.25\pi$ it decreases, while K_H at a_0 shows complex nature with the increment in θ. Similarly, Figure 4.2.3b shows that the heat flux intensity factor at the crack tip $-a_0$ initially increases as the crack orientation angle θ varies from 0 to 0.25π but after that it decreases as θ increases. However in this case also K_H at a_0 shows monotonic nature for increasing values of θ. Under both components of heat flow, the magnitude of K_H at the right crack tip is greater than that at the left crack tip.

Figures 4.2.4 and 4.2.5 show the variations of mode I and mode II crack tip TSIFs for distinct values of θ under steady-state heat flow components. From

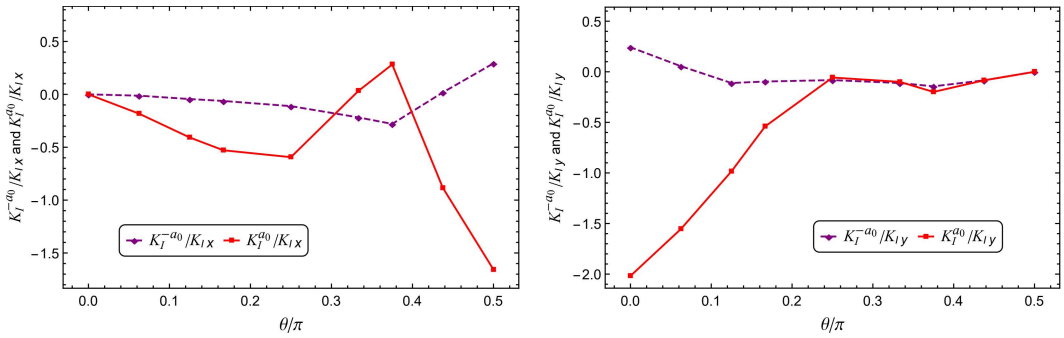

(a) **(b)**

Figure 4.2.4: Variations in normalized mode I crack tip TSIFs subjected to (a) horizontal and (b) vertical heat flow for distinct values of normalized crack orientation angle θ/π.

the comparison of Figures 4.2.4a and 4.2.4b, it is clear that the maximum value of the normalized crack tip K_I is obtained for horizontal heat flow. This indicates that the heat flow in the direction of material grading gives rise to the severe near-tip condition. Moreover, the negative values of K_I imply that there is a possibility of crack surface contact. Figures 4.2.5a and 4.2.5b illustrate that the magnitude of normalized K_{II} at the right crack tip is greater as compared to the left crack tip for both components of heat flow.

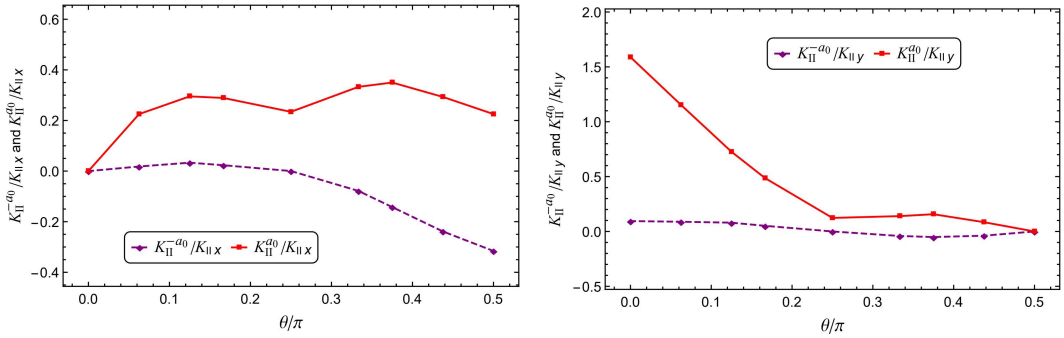

(a) **(b)**

Figure 4.2.5: Variations in normalized mode II crack tip TSIFs subjected to (a) horizontal and (b) vertical heat flow for distinct values of normalized crack orientation angle θ/π.

Therefore, the disturbance in heat flow in both directions is significantly

affected as the crack orientation angle changes from acute to obtuse. Also, if both the heat flow and material grading are in the same direction then the crack opening mode causes much disturbance in the flow of heat. Thus it is important to consider different values of θ instead of only $\theta = 0, \pi/2$.

4.2.6.3 Influence of biot number

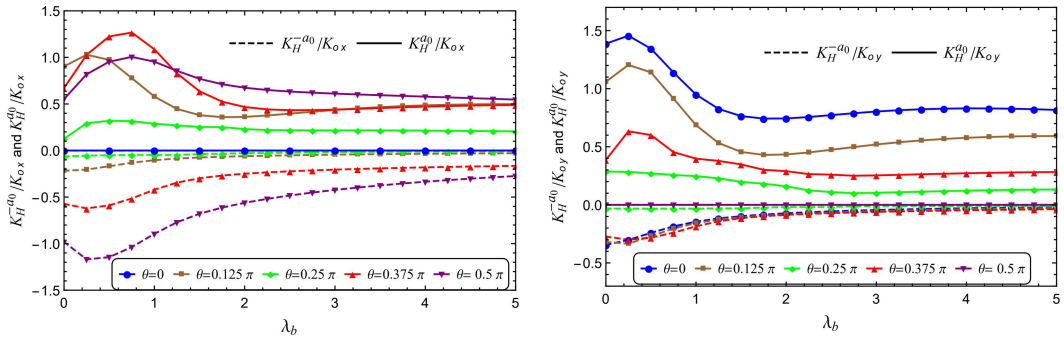

Figure 4.2.6: Plots showing normalized crack tip HFIFs as a function of biot number λ_b subjected to (a) horizontal and (b) vertical heat flow.

The behavior of HFIF at the crack tips $-a_0$ and a_0 under horizontal and vertical heat flow for $\theta = 0, 0.125\pi, 0.25\pi, 0.375\pi, 0.5\pi$ is displayed through Figure 4.2.6. From Figure 4.2.6a it is noted that in the presence of horizontal heat flow HFIF at the right crack tip initially increases as λ_b increases. After some fixed value of λ_b it started to decrease and for λ increasing from 2 to 5 the variation in HFIF becomes very small. This behavior is obtained for all distinct values of θ except $\theta = 0$, at which the magnitude of HFIF diminishes whatsoever the value of λ_b is taken. However, for HFIF at the left crack tip, the opposite trend is observed. Further, it can be observed from Figure 4.2.6a that under horizontal heat flow the difference in magnitude of left and right crack tip HFIFs is small. Analogously, from Figure 4.2.6b it can be noted that under vertical heat flow the trend of HFIFs at the crack tips is similar to that of horizontal heat flow as θ varies. But under this flow,

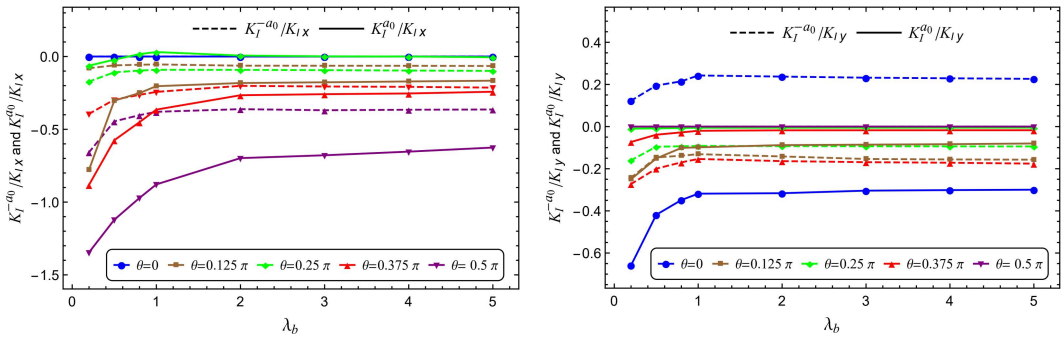

(a) **(b)**

Figure 4.2.7: Plots showing normalized mode I crack tip TSIFs as a function of biot number λ_b subjected to (a) horizontal and (b) vertical heat flow.

the magnitude of HFIF diminishes for any value of λ_b for the crack angle $\theta = 0.5\pi$. The variation in the magnitude of HFIF at the left crack tip becomes smaller with the change in crack obliquity. This is due to the effect of thermal conductivity on the adjacent constituent of the left crack tip.

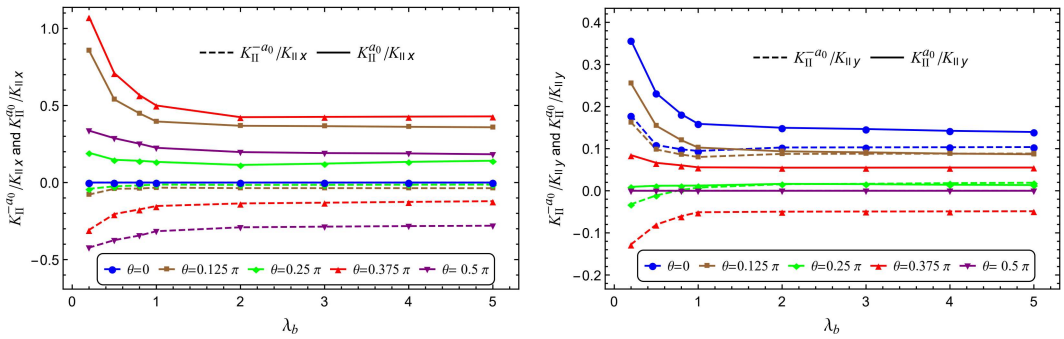

(a) **(b)**

Figure 4.2.8: Plots showing normalized mode II crack tip TSIFs as a function of biot number λ_b subjected to (a) horizontal and (b) vertical heat flow.

Figures 4.2.7 and 4.2.8 illustrate the effect of biot number on the normalized mode I and II crack tips' TSIFs under horizontal and vertical components of heat flow for different values of θ. As the nature of the perfectly insulated crack ($\lambda_b = 0$) changes to the partially insulated ($\lambda_b > 0$) one, the mode I crack tip TSIFs increase

and become almost constant when $\lambda_b > 1$ or 2. This shows that for large values of λ_b, the variation in the crack tip TSIFs is almost negligible. However, when steady-state heat flows horizontally the behavior of $K_{II}(-a_0)$ as a function of λ_b is similar to $K_I(-a_0)$ as θ varies whereas for $K_{II}(a_0)$ it is opposite in nature. Figure 4.2.8b indicates that an interesting behavior is obtained for normalized $K_{II}(-a_0)$ under vertical heat flow. As biot number increases from 0 to 1, the magnitude of $K_{II}(-a_0)$ decreases as the crack angle increases from 0 but after $\theta = 0.25\pi$, $K_{II}(-a_0)$ increases with the increase in λ_b. For $\lambda_b > 1$, the change in TSIFs at the left crack tip remains negligible for all values of θ. The variation of $K_{II}(a_0)$ under vertical heat flow is similar to that of $K_I(a_0)$ under horizontal heat flow.

4.2.6.4 Influence of width ratio

The effect of strips' width on the crack tip HFIFs is illustrated by Figure 4.2.9. It can be observed from Figure 4.2.9a that under horizontal heat flow as the ratio of the strips' width w_2/w_1 increases the magnitude of HFIF at the crack tip $-a_0$ increases while at the crack tip a_0 it decreases. Moreover, the trend of HFIF is the

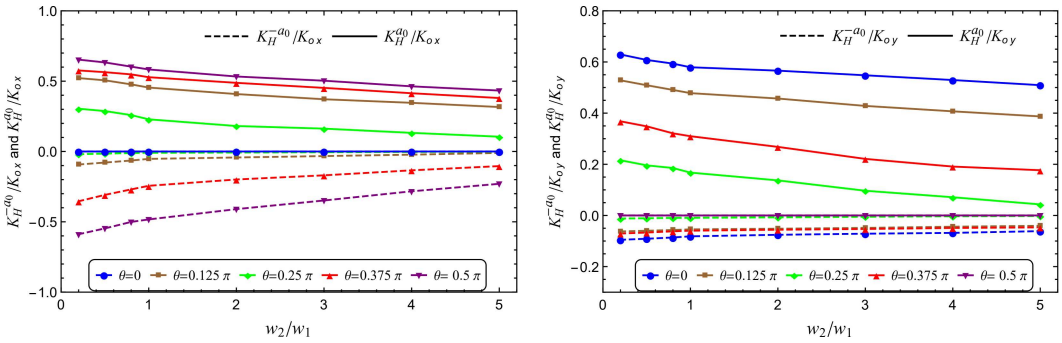

(a) **(b)**

Figure 4.2.9: Influence of width ratio w_2/w_1 on normalized crack tip HFIFs subjected to (a) horizontal and (b) vertical heat flow.

same for all θ at both crack tips except for $\theta = 0$. For the crack angle $\theta = 0$, the

magnitude of HFIFs is zero for any value of width ratio. The nature of crack tip HFIFs under vertical heat flow is the same as observed for horizontal heat flow as seen from Figure 4.2.9b except for $\theta = 0.5\pi$ for which HFIF diminishes. From the above discussion, it can be concluded that for wider strip (I) the magnitude of HFIF decreases for the left crack tip, while it increases for the right crack tip. Similarly, as the width of the strip (II) increases the intensity of heat flux increases at the left crack tip but decreases at the right crack tip. In other words wide strips are more effective in dissipating the heat in the near-tip region.

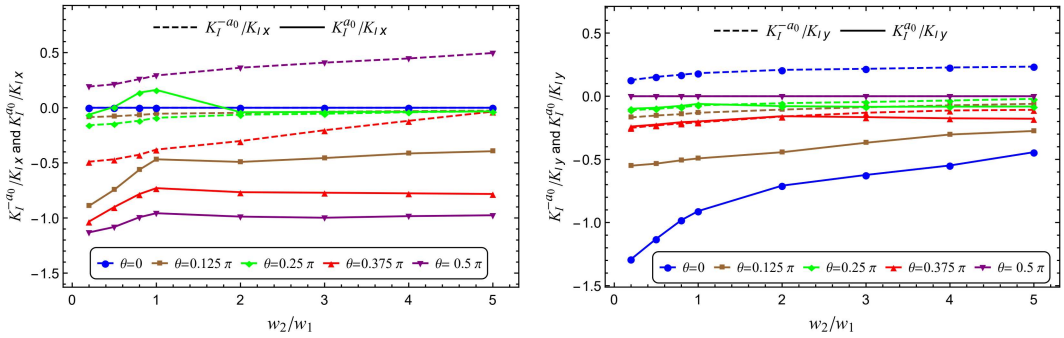

Figure 4.2.10: Influence of width ratio w_2/w_1 on normalized mode I crack tip TSIFs subjected to (a) horizontal and (b) vertical heat flow.

Figure 4.2.10 demonstrates the impact of strips' width on normalized K_I in the vicinity of the crack tip. It is seen from Figure 4.2.10a that under horizontal heat flow as the width of the strip (I) increases mode I TSIF at a_0 increases but as soon as the width of the strip (II) started to increase, mode I TSIF at a_0 decreases and shows small variation as the width increases further. The normalized K_I at the crack tip $-a_0$ increases as the w_2/w_1 increases or in other words as the width of the strip (I) decreases.

From the Figure 4.2.10b it can be said that when the heat flows vertically, the mode I TSIF at both crack tips increases as the width ratio w_2/w_1 increases

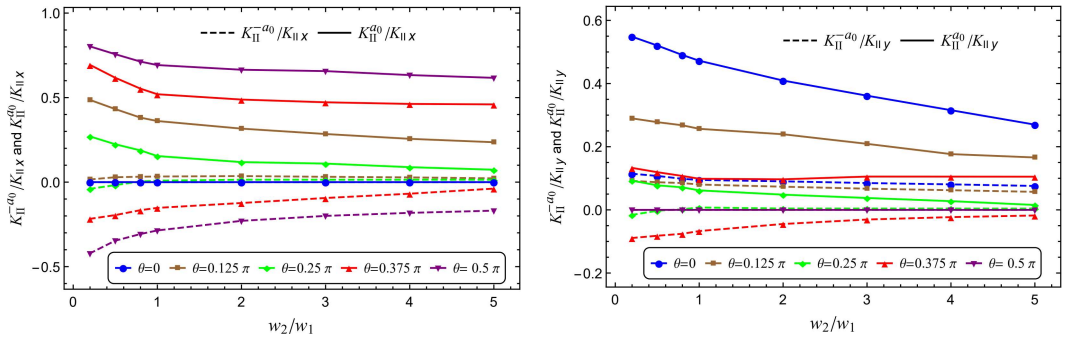

Figure 4.2.11: Influence of width ratio w_2/w_1 on normalized mode II crack tip TSIFs subjected to (a) horizontal and (b) vertical heat flow.

for $\theta = 0, 0.125\pi, 0.25\pi, 0.375\pi, 0.5\pi$. One can observe from Figure 4.2.11a that for horizontal heat flow as the width ratio increases or width of the strip (I) decreases, $K_{II}(-a_0)$ increases whereas $K_{II}(a_0)$ decreases for distinct values of θ. For normalized K_{II}, Figure 4.2.11b depicts that at the right crack tip the magnitude decreases with the increase in w_2/w_1 for almost all values of θ. However, for different values of the crack angle the behavior of $K_{II}(-a_0)$ is different.

4.2.6.5 Influence of nonhomogenity parameter ratios

Figures 4.2.12 to 4.2.18 demonstrate the impact of non-homogeneity parameters on the crack tip field intensity factors due to horizontal and vertical steady-state heat flow. From Figure 4.2.12a it is seen that under horizontal heat flow as δ_2/δ_1 increases from 0 to 1 the magnitude of HFIF at $-a_0$ decreases but as soon as the said ratio increases further from the value 1 the magnitude increases. However, the opposite trend is observed for HFIF at the crack tip a_0. Similarly, from Figure 4.2.12b, it is easy to observe that under vertical heat flow, the behavior of HFIF at both crack tips is the same as due to horizontal heat flow. Thus, it can be said that

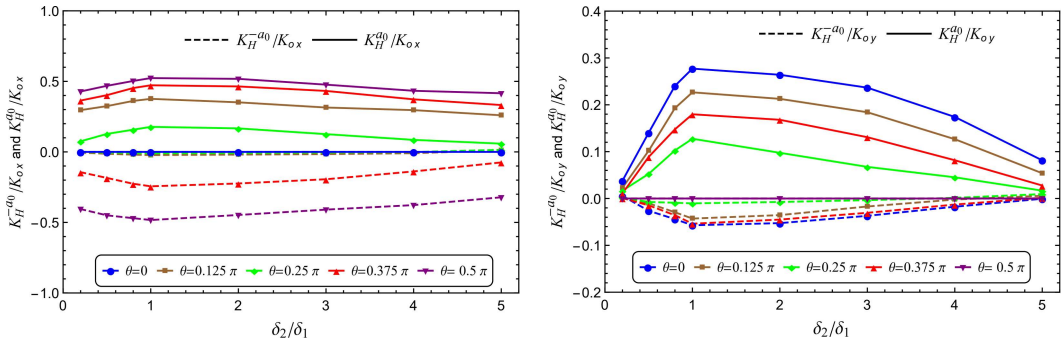

(a) **(b)**

Figure 4.2.12: Effect on normalized crack tip HFIFs of heat conduction parameter ratio δ_2/δ_1 subjected to (a) horizontal and (b) vertical heat flow.

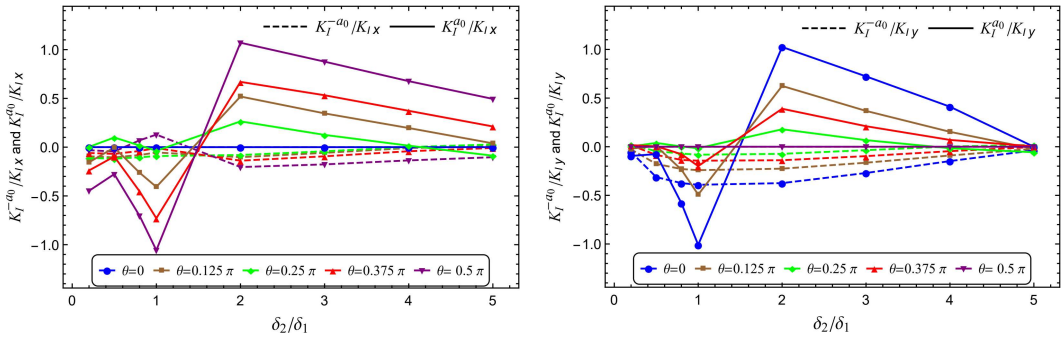

(a) **(b)**

Figure 4.2.13: Effect on normalized mode I crack tip TSIFs of heat conduction parameter ratio δ_2/δ_1 subjected to (a) horizontal and (b) vertical heat flow.

the heat dissipation is facilitated as the heat conductivity parameter of the material increases.

The result is displayed in Figures 4.2.13 and 4.2.14 manifest that as the heat conductivity of strip (I) increases the magnitude of normalized mode I TSIF at both crack tips changes significantly for both components of heat flow. For $\theta = 0, 0.125\pi, 0.25\pi, 0.375\pi, 0.5\pi$, K_{II} show monotonic behavior as the value of heat conduction parameter ratio increases. Further, it is found in Figures 4.2.13 and 4.2.14 that for varying values of heat conduction parameter the trend of both modes I and II TSIFs are different from each other. Therefore, thermoelastic singular

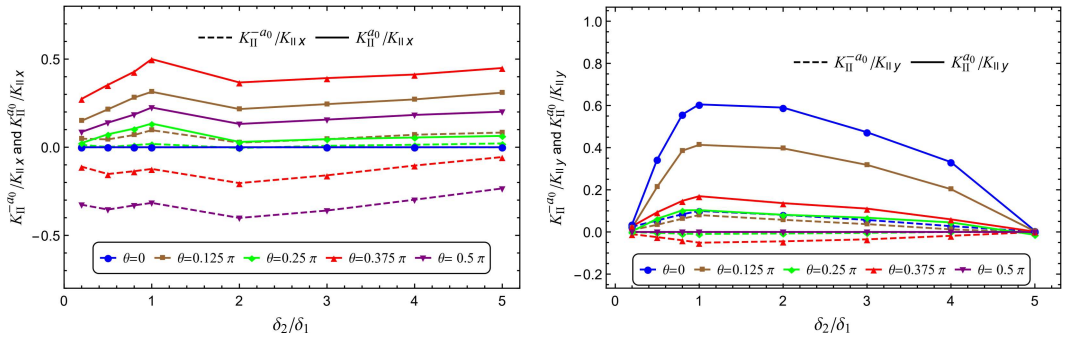

(a) **(b)**

Figure 4.2.14: Effect on normalized mode II crack tip TSIFs of heat conduction parameter ratio δ_2/δ_1 subjected to (a) horizontal and (b) vertical heat flow.

behavior for both opening and shearing mode is strongly affected by the heat conductivity parameter of the material. The demeanor of crack tip TSIFs under the

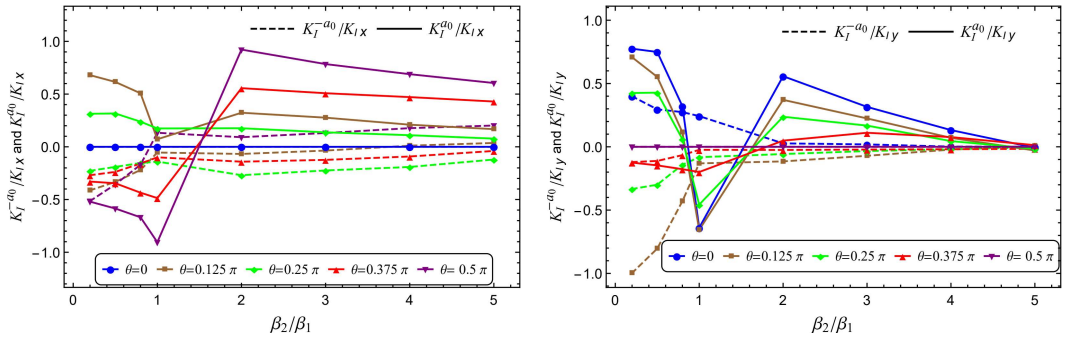

(a) **(b)**

Figure 4.2.15: Impact of stiffness parameter ratio β_2/β_1 on normalized mode I crack tip TSIFs subjected to (a) horizontal and (b) vertical heat flow.

horizontal and vertical components of heat flow is presented through Figures 4.2.15 and 4.2.16.

Figure 4.2.15a shows that when the crack obliquity varies from 0 to 0.5π, the intensity of $K_I(a_0)$ decreases as the stiffness of strip (II) increases under steady-state horizontal heat flow. Similarly for compliant strip (I), the mode I TSIF at the crack tip $-a_0$ becomes more intensified. Figure 4.2.15b shows that analogous

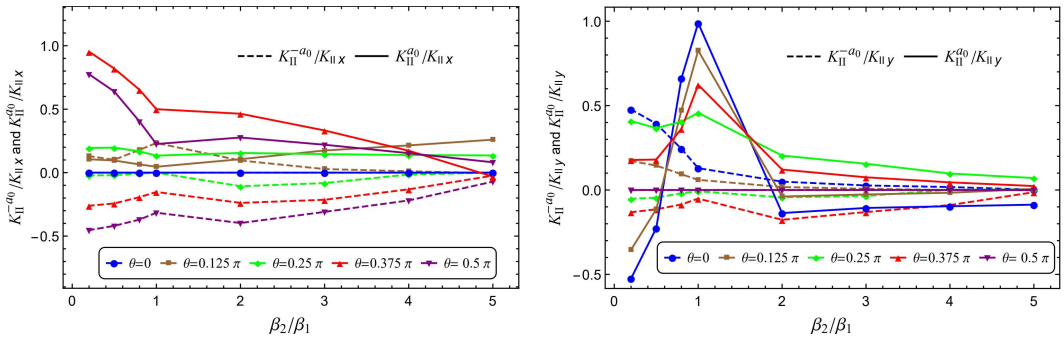

(a) **(b)**

Figure 4.2.16: Impact of stiffness parameter ratio β_2/β_1 on normalized mode II crack tip TSIFs subjected to (a) horizontal and (b) vertical heat flow.

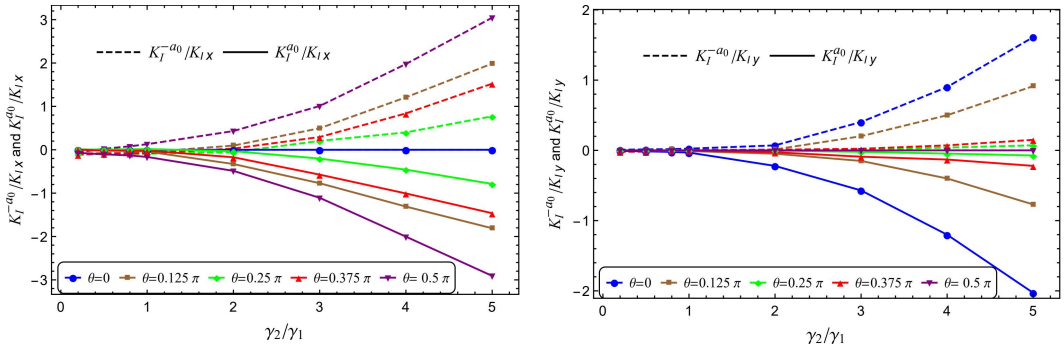

(a) **(b)**

Figure 4.2.17: Impact of thermal expansion coefficient ratio γ_2/γ_1 on normalized mode I crack tip TSIFs subjected to (a) horizontal and (b) vertical heat flow.

behavior is obtained for mode I crack tip TSIFs under vertical heat flow. From Figure 4.2.16 it can be concluded that for increasing stiffness parameter ratio β_2/β_1, the mode II crack tip TSIFs show similar behavior to mode I TSIFs. It is observed from Figures 4.2.17 and 4.2.18 that as the ratio of thermal expansion coefficient γ_2/γ_1 increases the absolute value of crack tip TSIFs increase for different values of θ except for $K_{II}(-a_0)$ under horizontal flow of heat component. Figure 4.2.18a shows that as the value of γ_2/γ_1 increases the monotonic behavior of $K_{II}(-a_0)$ changes for different θ.

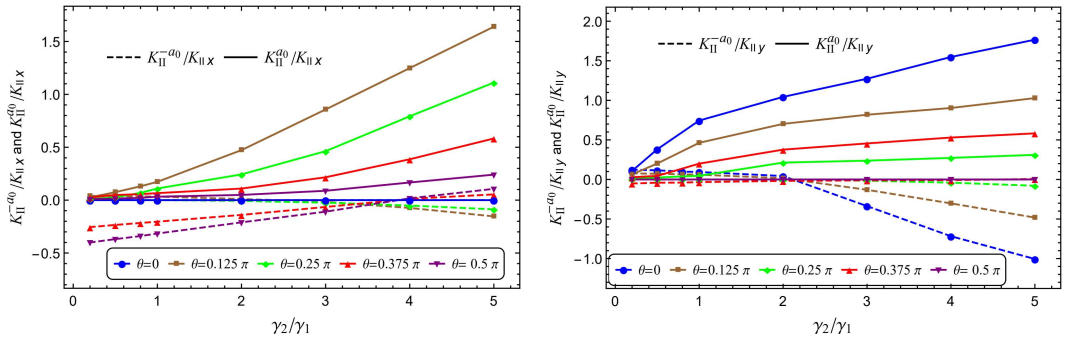

Figure 4.2.18: Impact of thermal expansion coefficient ratio γ_2/γ_1 on normalized mode II crack tip TSIFs subjected to (a) horizontal and (b) vertical heat flow.

4.2.7 Concluding remarks

This chapter focuses on the investigation of disturbances in steady-state heat flows brought on by an arbitrarily oriented crack crossing the interface. The centre of the crack is located at the interface of two bonded functionally graded strips. The findings of this study are as follows:

1. The Schmidt method is used to determine the analytical forms of the heat flux intensity factor, as well as the mode I and mode II thermal stress intensity factors close to the crack tips.

2. The crack's orientation angle affects the crack tip field intensity factors, and for both the horizontal and vertical components of steady-state heat flow, the field intensity factors at one crack tip differ from other. Furthermore, when the direction of heat flow and material grading is same, the extremum value of the crack tip K_I is obtained.

3. The intensities of the horizontal and vertical components of heat flow change monotonically when the crack's nature changes from completely insulated to

partially insulated. Further, the negative values of K_I give rise to the possibility of crack-surface contact.

4. The pictorial presentations of crack tip HFIFs under the impact of strips' width conclude that for the strip in which the tip of crack is located, the HFIF at that tip increases as the width of the said strip decreases. For different values of θ, the width of the strips has a significant impact on the mode I and mode II crack tip TSIFs.

5. The field intensity factors for horizontal and vertical heat flows exhibit an incremental-decremental nature with changes in the non-homogeneity of the FGM strips.

****